Maladaptive nutrient signalling sustains the m.3243A>G mtDNA mutation

Chih-Yao Chung[1], Kritarth Singh[1], Vassilios N Kotiadis[1], Jee Hwan Ahn[1], Lida Kabir[1], Emilie Topley[1], Joycelyn Tan[1], William D Andrews[1], Nicoletta Plotegher[1,2], Graziano Guella[3], Robert D S Pitceathly[4], Gyorgy Szabadkai[1,5,6], Mariia Yuneva[6], Michael R Duchen[1*]

1 Department of Cell and Developmental Biology and Consortium for Mitochondrial Research, UCL, Gower Street, London WC1E 6BT

2 Department of Biology, University of Padua, Padua, Italy

3 Bioorganic Chemistry Laboratory, Department of Physics, University of Trento, Trento, Italy

4 Department of Neuromuscular Diseases, UCL Queen Square Institute of Neurology and The National Hospital for Neurology and Neurosurgery

5 Department of Biomedical Sciences, University of Padua, Padua, Italy

6 The Francis Crick Institute, London

*Correspondence: m.duchen@ucl.ac.uk

Keywords: mitochondria; mtDNA; mtDNA mutations; nutrient signalling; m.3243A>G; PI3K; Akt; mTORC1; mitophagy

ABSTRACT

Mutations of the mitochondrial genome (mtDNA) cause a range of profoundly debilitating clinical conditions for which treatment options are limited. Most mtDNA diseases show heteroplasmy – tissues express both wild-type and mutant mtDNA. The relationships between specific mtDNA mutations, heteroplasmy, disease phenotype and severity are poorly understood. We have extensively characterised changes in bioenergetic, metabolomic, lipidomic and RNAseq profiles in heteroplasmic patient-derived cells carrying the m.3243A>G mtDNA mutation, the cause of mitochondrial encephalomyopathy, lactic acidosis and stroke-like episodes (MELAS). These studies reveal that the mutation promotes upregulation of the PI3K-Akt-mTORC1 axis in patient-derived cells and tissues. Remarkably, pharmacological inhibition of PI3K, Akt, or mTORC1 activated mitophagy, reduced mtDNA mutant load and rescued cellular bioenergetics cell-autonomously. The rescue was prevented by inhibition of mitophagy. These findings suggest that activation of the PI3K-Akt-mTORC1 axis is maladaptive and represents a potential therapeutic target for people suffering from the consequences of the m.3243A>G mutation.

INTRODUCTION

Mitochondria control cellular bioenergetic homeostasis and serve as a hub for cell metabolism and cell signalling pathways. Human mitochondria contain a circular plasmid-like DNA (mtDNA) which encodes 13 proteins which act as subunits of the electron transport chain (ETC) and 24 RNAs essential for mitochondrial protein synthesis. Mutations of mtDNA affect around 1 in 5000 of the population[1] and cause a range of diseases for which no effective treatment is available[2,3]. Over half of the known pathogenic mutations are found within tRNA genes, in which the m.3243A>G mutation, a $tRNA^{Leu}$ point mutation accounts for about 40% of adult patients of primary mitochondrial diseases[1,4]. Clinically, patient symptoms associated with mtDNA mutations are highly heterogeneous[2,5]. The tissues primarily affected vary depending on the specific mtDNA mutations, and our understanding of the relationships between mtDNA mutations, disease phenotype and severity is still very limited[2,3]. The majority of diseases caused by mutations of mtDNA are heteroplasmic – tissues express both normal and mutation carrying mtDNA. This is a confounding complication, as disease expression may differ radically between patients with the same mutation but different mutant load. While disease severity broadly correlates positively with the relative burden of mutant mtDNA, we know remarkably little about the determinants of the mutant mtDNA burden[3,6–8].

Mitochondrial quality control pathways, including mitophagy, mitochondrial biogenesis pathways and mitochondrial shaping mechanisms, are critically involved in regulating mitochondrial energy homeostasis[9,10]. Several studies have demonstrated the accumulation of damaged mitochondria and defective mitophagy as a hallmark of mtDNA diseases and age-related neurodegeneration, suggesting that the presence of pathogenic mtDNA alone is not sufficient to drive selection against the mutation by the activation of mitophagy[11–15]. We therefore asked how cell signalling pathways influence these pathways in the disease model, as adaptive - or maladaptive – responses to impaired oxidative phosphorylation (OxPhos) and changes in intermediary metabolism, and whether these pathways play a role as determinants of mutant load and disease severity.

Here, we have characterised the metabolic phenotype of patient-derived cells bearing the m.3243A>G ($tRNA^{Leu}$) mutation. This is the most common heteroplasmic mtDNA mutation[1,4], and, clinically, is expressed variably but may include diabetes, sensorineural deafness, myopathy, encephalopathy, lactic acidosis and stroke-like episodes (MELAS). We have found that the expression and activity of the PI3K-Akt-mTORC1 pathway were increased in the mutant cells, and was strongly associated with redox imbalance, oxidative stress, and glucose dependence. Phosphorylation of Akt and ribosomal protein S6 (a downstream target of mTORC1) were also increased in muscle biopsies from other patients with the mutation, confirming that this signalling pathway is constitutively activated in

patient tissues. Remarkably, inhibition of PI3K, Akt, or mTORC1 all substantially reduced mutant load and rescued mitochondrial bioenergetic function. We found that this process is mediated by upregulation of mitophagy which is absolutely required for rescue of mitochondrial function and reduction in mutant load. Our study reveals that in response to the m.3243A>G mutation, metabolism is rewired, and activity of the PI3K-Akt-mTORC1 axis is increased, as an adaptive response to metabolic changes driven by the mutation. The finding that inhibition of the pathway reduces mutant load and rescues function suggests that activation of this signalling pathway is, in fact, maladaptive, that activation of the pathway sustains disease progression and that pharmacological intervention in this signalling pathway represents a potential therapeutic strategy in patients with these dreadful diseases.

RESULTS

The m.3243A>G mutation causes mitochondrial dysfunction and glucose dependence, resulting in redox imbalance and oxidative stress.

To explore the metabolic and cell signalling impact of the m.3243A>G mutation, we used six cell lines: fibroblasts derived from two patients carrying the mutation, two controls matched for age and gender, an A549 cybrid cell line carrying the mutation and its Wild-type (WT) counterpart. PCR-RFLP[16] and ARM-qPCR[17] were used to quantify the m.3243A>G mutation load in these cell models. One patient-derived line (henceforth referred to as patient 1) showed a mutant load of 86.2 ± 2.3%; a second line (referred to as patient 2) showed a mutant load of 30.3 ± 3.5%, and the mutant load was 79.0 ± 0.3% in the cybrid cells (Fig. 1A; for more details about the patients please see Methods).

To characterise the metabolic phenotype of the mutant cells, respiratory rate was measured using the Seahorse XFe96 extracellular flux analyser. These measurements showed a profound decrease in resting respiratory rate, ATP dependent respiration and in maximal respiratory capacity in both patient lines (Fig. 1B, D). Respiratory rates were also significantly reduced in the cybrid cells, when normalised to their increased mtDNA copy number (Fig. S1A), compared to the control A549 cells (Fig. 1C-D). In line with these findings, immunoblotting of respiratory chain supercomplexes using blue native gels electrophoresis (BNGE), which identify macromolecular assemblies, revealed disrupted expression of respiratory chain proteins in the mutant cells (Fig. 1E). Notably, there was a very large decrease in supercomplex I_2+ III_2 +IV_n, III_2+IV_1 and III_2/IV_2 assembly and in complex IV_1 (Fig. 1E). Mitochondrial membrane potential ($\Delta\psi_m$) was reduced in both patient-derived fibroblast lines (Fig. 1F) and the cybrid cells (Fig. S1B). The decrease in $\Delta\psi_m$ was significantly greater in cells from patient 1 than from patient 2, consistent with the greater mutant load in patient 1. Mitochondrial morphology was also altered in patient fibroblasts, showing significant fragmentation of the mitochondrial network, which was more severe in cells from patient 1 than from patient 2 (Fig. 1F).

Mitochondrial dysfunction may alter rates of free radical generation by the respiratory chain. The rate of increase of dihydroethidium (DHE) fluorescence (Fig. S1C), reflecting the intracellular rate of production of reactive oxygen species (ROS), was significantly increased both in patient fibroblasts and in the cybrid cells, compared to matched controls (Fig. 1G and S1D). MitoSOX, a mitochondria-targeted form of DHE, revealed a significant increase in the rate of ROS generation in the mitochondria in the mutant cells (Fig. 1G, ii; Fig. S1D, ii), suggesting that the increased rate of ROS generation is likely the consequence of an impaired respiratory chain. Together, the m.3243A>G mutation results in mitochondrial dysfunction, mitochondrial fragmentation and elevated ROS generation.

We wondered whether glucose metabolism is altered in the mutant cells, supporting their bioenergetic homeostasis and compensating for the mitochondrial dysfunction. Using time-lapse live-cell imaging, we quantified cell growth rates by fitting the curves of cell confluence with an exponential cell growth model (Fig. S1E) under a variety of nutrient conditions. Growth rates were significantly reduced in all mutant fibroblasts compared to their control counterparts (Fig. S1F). Moreover, the cell proliferation rate was significantly reduced in all mutant cells in 1 and 5 mM glucose media (Fig. 1H and S1G) but not in low concentrations of glutamine, suggesting that the patient-derived cells are significantly more dependent on glucose metabolism. Consistently, the rate of uptake of the fluorescent glucose analogue, 2-NBDG, was significantly increased in both patient fibroblasts and the cybrid cells, compared to controls (Fig. 1I and S1H).

The cytosolic NADH:NAD^+ ratio is a function of glycolytic flux (which consumes NAD^+, generating NADH), lactate production through lactate dehydrogenase (LDH) which produces lactate and regenerates NAD^+ from NADH and the activity of malate/aspartate and the glycerol phosphate shuttles that exchange NADH and NAD^+ between cytosol and mitochondrial matrix (Fig. 1J). We used the genetically encoded reporter SoNar[18] to quantify the cytosolic NADH:NAD^+ ratio (Fig. S1I). The basal NADH:NAD^+ ratio was significantly increased in the patient fibroblasts and cybrid cells compared to controls, consistent with reduced mitochondrial activity and higher glucose catabolism through glycolysis (Fig. 1K and S1J). It was also consistent with significantly higher levels of lactate produced by the patient fibroblasts compared to controls (Fig. 1L). The pH of the growth media, reflecting cellular lactate production, was also measured using the absorbance of phenol red. The acidification of media by mutant cells was significantly greater than that of controls (Fig S1K). These data recapitulate the lactic acidosis which is characteristic of patients with the m.3243A>G mutation[19], and suggest that in patient fibroblasts, increased activity of LDH may compensate for the decreased regeneration of NAD^+ by mitochondria, supporting increased glycolytic flux. Addition of exogenous pyruvate can support mitochondrial activity, increasing OxPhos, and stimulate LDH activity to generate lactate, changing the NADH:NAD^+ ratio. In control cells, pyruvate addition decreased the cytosolic NADH:NAD^+ ratio, but had a negligible effect on the high NADH:NAD+ ratio in mutant cells (Fig. 1K and S1J), suggesting that in the latter, LDH flux is already operating at its maximum capacity. Together, these data confirm that in the mutant cells, decreased mitochondrial activity results in higher glucose uptake, glucose catabolism into lactate and increased cytosolic NADH:NAD^+ ratio.

The m.3243A>G mutation remodels glucose and lipid metabolism towards increased anabolic biosynthesis and lipid accumulation.

To investigate the glucose-dependent metabolic alterations in the mutant cells and identify metabolic signals which might result in cell signalling changes, glucose uniformly labelled with isotopic carbon ([U-^{13}C]-glucose) was used to trace its metabolic fate in the cells by gas chromatography-mass spectrometry (GC-MS). The pattern and abundance of ^{13}C enrichment in downstream metabolites were used to determine the relative contribution of glucose into different metabolic pathways. First, partial least squares discriminant analysis (PLS-DA) for the concentration of metabolites (Fig. S2A) showed a clear separation between patient fibroblasts and controls (Fig. S2B). The analysis of metabolic pathways revealed enrichment of lipid metabolism, pentose phosphate pathway (PPP), glycolysis and the tricarboxylic acid (TCA) cycle (Fig. 2A). Tracing the fate of ^{13}C-glucose through glycolysis (Fig. 2B), we found that the enrichment of ^{13}C in glucose-6-phosphate (G6P) in the mutant cells was at a similar level as in controls (Fig 2B), but the total pools of G6P were increased (Fig. S2A) consistent with increased glucose uptake. Although the end products of glycolysis, intracellular pools of pyruvate and lactate in the mutant cells, were maintained at similar levels with controls in terms of ^{13}C enrichments and concentrations (Fig. 2B and S2A), the levels and the ^{13}C enrichment of glycerol-3-phosphate (G3P) were increased. The latter suggests the increased activity of glycerol-3-phosphate dehydrogenase in response to increased cytosolic NADH/NAD$^+$ ratio, which may drive elevated lipid biosynthesis (Fig. 2B). Interestingly, the levels of alanine were increased but its ^{13}C enrichment was decreased, suggesting a contribution from other nutrient sources. Similarly, the total amount of serine was increased in patient fibroblasts, despite decreased synthesis of serine from glucose, suggesting increased serine uptake from extracellular media (Fig. 2B, S2A and S2C).

Consistent with OxPhos defects, levels of the TCA cycle intermediates, malate, fumarate and succinate, were decreased in the mutant cells, while the levels of citrate were increased (Fig. S2A). Interestingly, the enrichment of m+3 isotopologues of these TCA cycle intermediates and aspartate were significantly increased in the mutant cells (Fig. 2B). To enter the TCA cycle, glucose-derived pyruvate is converted into acetyl-CoA by pyruvate dehydrogenase (PDH). In this case the catabolism of [U-^{13}C]-glucose results in m+2 enrichment of TCA cycle intermediates, including oxaloacetate (OAA), a precursor of aspartate. In contrast, m+3 isotopologues of TCA cycle intermediates are generated if pyruvate is converted into OAA by pyruvate carboxylase (PC). Metabolite set enrichment analysis of the metabolomics data also predicted that PC is affected (Fig. S2D). Immunoblotting for phospho-PDH and PC expression revealed elevated PC expression and increased levels of phosphorylated PDH (indicating its reduced activity) in both patient fibroblasts and cybrid cells (Fig. 2C). As the glucose contribution into the TCA cycle is usually low in conventional cell culture systems, this slight but significant difference in the enrichment of ^{13}C is meaningful. The switch from PDH to PC as means of channelling glucose-derived carbon into the TCA cycle in mutant fibroblasts is consistent with the

increased NADH/NAD+ ratio, which stimulates the activity of pyruvate dehydrogenase kinase, phosphorylating PDH and inhibiting its activity.

As increased levels and glucose-derived enrichment of G3P suggest increased lipid biosynthesis, we asked whether lipid metabolism is altered in the mutant cells. Nile Red O staining, which labels neutral lipids, showed a substantial and significant accumulation of lipid droplets in the mutant cells, increasing both the number and the area of droplets (Fig. 2D). Interestingly, accumulation of lipid droplets has also been seen in biopsies from patients with MELAS[20]. A systematic lipidomic analysis using LC-MS showed that lipid profiles of patient fibroblasts were distinct from the controls, with a striking increase in membrane and storage lipids, including glycerophosphatidylinositols, cholesteryl esters and sphingomyelins (Fig. 2E). PLS-DA again showed a clear separation of lipidomic profile between patient and control fibroblasts (Fig. S2E). Similarly, the enrichment of metabolic pathways from the lipidomic data revealed upregulation of processes involved in membrane lipid metabolism and signalling systems (Fig. S2F). Our findings from the stable-isotope-labelling approach and comparative metabolomics thus reveal a profound remodelling of glucose and lipid metabolism as a consequence of OxPhos defects arising from the m.3243A>G mutation.

The chronic activation of PI3K-Akt-mTORC1 in the m.3243A>G mutant cells impairs autophagy and induces a deleterious integrated stress response

The metabolic phenotype shown above points to reprogramming of nutrient-sensing signalling networks in the m.3243A>G mutant cells. We therefore carried out an RNA sequencing screen to examine global changes in the expression profiles of the patient fibroblasts. Using a significance level of false discovery rate (FDR) < 0.05, we identified 3394 transcripts of which 1849 were upregulated and 1545 were downregulated. A multi-dimensional principal component analysis also confirmed good accordance between biological triplicates as well as close clustering of transcripts from patient fibroblasts (Fig. S3A-C). The enrichment analysis of these differentially expressed genes identified 'mitochondrial dysfunction', 'superoxide radical degradation', 'Cholesterol biosynthesis' as the top-scoring pathways in patient fibroblasts (Fig. 3A). Analysis of individual genes involved in these pathways showed a general downregulation of OxPhos genes (Fig. S3D), but increased expression of genes involved in oxidative stress defence pathways and membrane lipid synthesis/remodelling (Fig. S3E-F). Specifically, the increased expression of PC was consistent with the immunoblotting data (Fig. 2C) and correlated with altered TCA cycle activity (Fig. S3G). The enhancement of glycolytic flux in the mutant cells reported by the metabolomic data was supported by the increased expression of

hexokinase 1 (HK1). These findings further validated the metabolic footprint observed in patient-derived cells from the metabolomic studies.

Consistent with the above results, the network analysis of upregulated genes identified the strong enrichment of NRF2 signalling as well as PI3K-Akt and mTOR pathways in patient fibroblasts (Fig. 3B and Fig. S4A; Table S1). We next validated these data at the protein expression level. Immunoblotting confirmed increased phosphorylation of Akt compared to total Akt, as well as the downstream mTORC1 target S6 ribosomal protein in patient fibroblasts (Fig. 3C) and the cybrid cells (Fig. S4B). While control fibroblasts showed a growth factor-dependent Akt activation in response to increased serum concentration in growth media, phospho-Akt was elevated in patient cells even when growth factors were low (1% FBS) and increased only slightly in response to an elevated serum concentration. Similarly, the patient fibroblasts exhibited increased mTORC1 activation independently of the serum concentration, revealed by increased phospho-S6 levels. PI3K-Akt-mTORC1 signalling also antagonizes the activity of the cellular energy sensor, AMP-activated protein kinase (AMPK) and suppresses macromolecular catabolism by autophagy. We therefore measured AMPK phosphorylation in response to different serum concentration by immunoblotting, but found no significant difference between patient and control fibroblasts. These results suggest that the constitutive induction of PI3K-Akt-mTORC1 signalling remodels cell metabolism, independently of growth factor stimulation.

We next explored the impact of chronic induction of PI3K-Akt-mTORC1 signalling on autophagic flux in the mutant cells (Fig. 3D)[13,21]. We monitored LC3B turnover in the presence and absence of chloroquine (CQ) using LC3B immunoblotting. The mutant cells showed an increased conversion to LC3BI to LC3BII form (autophagosome) but the difference in LC3BII accumulation in the presence of CQ was not significantly different between control and mutant cells (Fig. 3E and S4C), indicating a defect in the late stage of autophagosome to autolysosome conversion/fusion in mutant cells. We also measured the autophagic flux using a mCherry-EGFP-LC3B tandem reporter[22] by live-cell imaging. Consistent with the above result, the ratio of green/red puncta was low in control compared to patient cells, representing the formation of mature autolysosomes and a high autophagy flux. In contrast, the ratio of green/red puncta and both the number and size of double-positive puncta were increased in mutant cells, indicating impaired autophagosome maturation into autolysosomes (Fig. 3F and S4D). Altogether, these results confirm that autophagic flux is impaired in the mutant cells and further indicate that an autophagy imbalance may contribute to metabolic and proteostatic stress in PI3K-Akt-mTORC1 activated cells.

Indeed, the network analysis of downregulated genes identified EIF2 and PTEN signalling as the top downregulated pathways (Fig. 3B). PTEN is a negative regulator of the PI3K-Akt-mTORC1 axis. Interestingly, inhibition of EIF2 signalling, a hub for the integrated stress response (ISR) and regulation

of protein translation under stress, in the m.3243A>G mutant cells indicated an attenuation of protein synthesis and induction of ISR[23,24]. Analysis of the individual transcripts from EIF2 signalling pathway showed a general downregulation of genes involved in ribosomal biogenesis and upregulation of transcription factors – ATF4, ATF5 and DDIT3 (CHOP) (Fig. S4A; Table S2-3). ATF4 acts as a prototypical downstream target coupling mitochondrial proteotoxic stress to the activation of ISR[25]. We therefore examined the protein expression levels of these genes to demonstrate the activation of the ISR in patient-derived cells. A significant increase in the phosphorylation levels of translation factor, eIF2α as well as the downstream targets, ATF4, ATF5 and CHOP confirmed the induction of the ISR in the mutant cells (Fig. 3G and Fig. S4E).

To establish that the PI3K-Akt-mTORC1 axis is constitutively active in patients with the m.3243A>G mtDNA mutation, we measured p-Akt/Akt and p-S6/S6 by immunofluorescence in a muscle biopsy from a patient with an 82% mutant load of the m.3243A>G mutation causing MELAS, (not one of the donors used to obtain the fibroblasts). A significant increase in p-Akt and p-S6 in the muscle biopsy argues that upregulation of this pathway is a clinical feature of the disease and not a specific function of the cultured cells (Fig. 3H). Re-analysis of a published RNA-seq data set[26] from muscle biopsies of MELAS patients also confirmed alterations in cholesterol and serine biosynthesis (Fig. 3I) and the activation of PI3K-Akt-mTORC1 signalling and induction of ISR in patients (Table S4). Although activation of the ISR has been proposed to be cytoprotective and promote longevity[27,28], our data suggest that the activation of ISR in the context of the m.3243A>G mtDNA mutation is not protective. Combined mitochondrial dysfunction, metabolic remodelling and impaired autophagy may act as an overarching inducer of ISR in PI3K-Akt-mTORC1 activated m.3243A>G mutant cells[29].

Pharmacological inhibition of PI3K-Akt-mTORC1 signalling reduces mutant load, resolves ISR, rescues mitochondria function and lowers glucose dependence in the m.3243A>G mutant cells

At this point, we asked what the functional consequences of the activation of the PI3K-Akt-mTORC1 axis are and whether it represents an adaptation to impaired OxPhos. We therefore systematically inhibited each component of the axis in turn using well-established pharmacological inhibitors (Fig. 4A)[21] and explored the consequences for mutant mtDNA burden and the pathophysiological and biochemical features that we have described above.

In both the fibroblasts from patient 1 and the cybrid cells, treatment with LY294002 (referred to below as 'LY', 5 μM, an inhibitor of PI3K) or with rapamycin (referred to as 'RP', 5 μM, the canonical inhibitor of mTORC1) led to a progressive decrease in mutant mtDNA load over 12 weeks of sustained treatment (Fig. 4B). The efficacy of each drug as the inhibitor of the PI3K-Akt-mTORC1 axis was

confirmed by immunoblotting the downstream kinase targets, showing significant changes in phosphorylated to unphosphorylated forms. Interestingly, in the absence of RP or LY, the fibroblasts from patient 2 showed a progressive increase in mutant load with time in culture, rising from ~30% to around 70% over 3 months (Fig. 4B). Treatment with the inhibitors significantly suppressed the rate of increase in mutant load decreasing the total change by around 20%. Although the decrease in mutant load took many weeks to develop, changes in protein phosphorylation state were evident within a day of starting treatment (Fig. 4C and S5A). Accordingly, inhibition of PI3K by LY reduced p-Akt/Akt ratio and mTOR phosphorylation, while rapamycin inhibited mTOR phosphorylation but had no impact on Akt. None of the treatments had any immediate effect on AMPK phosphorylation. However, AMPK activity gradually increased at later time points after drug treatments, suggesting an induction of catabolic processes such as autophagy and improvement in sensing the bioenergetic status of the m.3243A>G mutant cells[30]. The ISR/UPR^{mt} pathway also changed accordingly after the drug treatments (Fig. 4C and S5B), which restored the expression of ATF4 and ATF5 to levels that were comparable to that of control. In LY-treated cells, ATF4 and ATF5 were downregulated almost immediately, while, interestingly, in RP-treated cells, ATF4 and ATF5 were decreased after a week of treatment. These data confirmed that the PI3K-Akt-mTORC1 axis is an upstream regulator of ISR[23,31], although the mechanisms by which inhibition of mTORC1 or PI3K/Akt resolves the ISR may differ[29].

To investigate whether the decrease in mutant load and suppression of ISR after drug treatment were reflected by a concomitant change in mitochondrial function, we measured the mitochondrial bioenergetic status and the metabolic phenotype of the patient-derived cells. Measurements of mitochondrial membrane potential showed a complete recovery to levels that were not significantly different from control cells (Fig. 4D and S5C). These changes were accompanied by a decrease in the fragmented phenotype in the mutant cells and a significant elongation and reformation of a mitochondrial network (Fig. 4D and S4C). Measurements of mitochondrial respiration showed that both basal and maximal respiratory capacity were increased in cells treated with LY or RP (Fig. 4E and S5D). Treatment of mutant cells with MK2206 (MK, 1 μM), a pan Akt inhibitor, also caused a progressive decrease in mutation load and restored mitochondrial function (Fig. S5E-I). We also examined the effects of LY and RP in cells carrying another heteroplasmic mtDNA point mutation – the m.8993T>G – generated by the Minczuk lab[27]. In these cells, inhibition of the PI3K-Akt-mTORC1 axis had no impact on mutant load (Fig. S5J), suggesting that hyperactivation of the PI3K-Akt-mTORC1 axis is relatively disease specific.

The improvement in mitochondrial respiration suggested a metabolic shift towards OxPhos. Measurements of cytosolic redox state using SoNar (Fig. 4F and S5K) showed a significant reduction in basal NADH:NAD$^+$ ratio and increased response to pyruvate addition in the long-term treated

patient-derived cells, implying a decreased glycolytic flux. Measurements of glucose and lactate concentration in the media showed a profound decrease in lactate secretion following LY and RP treatments (Fig 4G and S5L). The cells were also cultured in media containing glucose or galactose as a primary carbon source to further assess their dependence on glycolysis. LY- and RP-treated cells, but not mutant controls, grew well in the galactose media, indicating a reduced glycolytic dependence after the drug treatments (Fig. 4H). Also, the mutant cells showed an increased supercomplex formation as well as individual components of the mitochondrial ETC following drug treatments (Fig. 4I). In Gel activity assay for CI and CIII+CIV revealed a significant increase in enzyme activity of ETC in response to the inhibitors (Fig. S5M). Further, the rates of ROS production were also reduced in cells treated with LY and RP (Fig. 4J and S5N). Altogether, our results demonstrate that the long-term treatment of the mutant cells with either LY or RP reverses the biochemical consequences of the mutation, rescuing mitochondrial function, reducing glucose dependence and decreasing the mutation load. These data strongly argue that the chronic activation of the PI3K-Akt-mTORC1 axis, presumably as an adaptive response to impaired oxidative metabolism, instead serves as a maladaptive response in this disease model.

Reduction of the m.3243A>G mutant load by inhibition of the PI3K-Akt-mTORC1 axis is cell-autonomous

The chronic activation of the PI3K-Akt-mTORC1 axis and increased mutant load have deleterious effects on cellular function and amplify the pathophysiological consequences of the mutation. However, this raises questions about the underlying mechanism by which inhibition of the axis reduces mutant load and rescues mitochondrial function. A possible explanation for the response to drug treatments is that inhibition of the signalling pathway may promote the selective growth of cell populations with low mutant load or selective elimination of cells with high mutant loads. We therefore carried out long term measurements of growth rates and cell death (Fig. 5A, i and ii). Although treatment with either LY or RP significantly slowed cell proliferation in both fibroblast and cybrid cells (Fig. 5B, upper panel), the changes were small. The cell growth rate was stable in cybrid cells treated with LY or RP, suggesting that there was no clonal expansion. In fibroblasts, growth rates of cells were not altered by treatment with drugs for 4 or 8 weeks, while a significant decrease of mutation load was clearly established after 4 weeks of treatment. This suggests that the change of mutation load is independent of the rate of cell growth. Cell death rates in the drug-treated groups were even lower than in the mutant controls, suggesting that the drug treatments were beneficial, and there was no selective killing of mutant cells (Fig. 5B, lower panel). Treating the mutant cells with MK showed similar results in terms of cell growth and death (Fig. S5A).

To determine definitively whether the reduction of mutant load in response to the drug treatments is cell-autonomous, we used a PCR-based technique, TaqMan SNP genotyping, at single-cell resolution to measure the distributions of the m.3243A>G heteroplasmy in a cell population (Fig. 5Aiii). The TaqMan technique was first validated by measuring the mutation loads of a population of cells and then to establish the range of single-cell mutant load across the population (Fig. S6B). The distribution of mutant load in the cybrid cells ranged from 50-80%, showing a Gaussian distribution (Fig. S6C). The average single-cell mutant load was consistent with that of the whole cell population. Measurement of the relative m.3243A>G heteroplasmy in patient fibroblasts and cybrid cells following treatment with LY and RP for 6 and 12 weeks respectively showed a frequency distribution which clearly segregated the treated group as a distinct population from the untreated group (Figs. 5C-D). The distribution of the mutant load in treated groups, although showing stochastic variation within the population, shifted to significantly lower levels compared to the untreated group. To determine whether the reduction in the burden of the m.3243A>G heteroplasmy is also phenocopied at the protein expression level, we immunostained the mtDNA-encoded cytochrome c oxidase I (MT-COI) in patient 1 fibroblasts. The presence of 7 UUA-encoded leucine residues within MT-COI renders the m.3243A>G $tRNA^{Leu(UUR)}$ cells prone to codon-specific translational defect[32]. Immunofluorescence staining revealed a significant decrease in MT-COI expression in patient 1 fibroblasts compared to controls (Fig. S6D). Following drug treatments, these cells showed a partial but significant recovery of MT-COI expression. The single-cell analysis of MT-COI expression segregated the drug-treated and untreated groups in a distribution pattern similar to the m.3243A>G proportion in Fig. 5D. A diminished expression of MT-COI also correlated with the lower assembly and activity of supercomplexes in Fig. 4I. Together, these results strongly suggest that rather than the enrichment of a specific cell population, the reduction in m.3243A>G heteroplasmy caused by inhibition of PI3K-Akt-mTORC1 signalling operates across the whole population and is likely cell-autonomous.

Restoration of autophagic/mitophagic flux by PI3K-Akt-mTORC1 inhibition is necessary to reduce the m.3243A>G mutant load.

Our results from the single-cell analysis strongly argue that the change in heteroplasmy is a cell-autonomous phenomenon. We then asked what mechanisms select against the mutant mtDNA. A possible explanation could be the elimination of the mutant mtDNA by reducing the total mtDNA copy number and then amplifying the dominant mtDNA, resembling 'the bottleneck' effect – the selection mechanism of mtDNA in germline or embryo[4,6]. We therefore quantified the total mtDNA copy number of the drug-treated cells at a series of time points, but no significant changes were seen

between the mutant control and drug-treated cells (Fig. S7A) and the total mtDNA copy number remained stable across the duration of drug treatments.

It also seemed plausible that the removal of dysfunctional mitochondria via mitophagy may reduce the mutant load in cells with the mtDNA mutation[33,34]. Indeed, long-term treatment with either RP or LY significantly increased the conversion and accumulation of LC3BII (autophagosome) in the presence of CQ compared to untreated cells (Fig. 6A and Fig. S7B). Notably, the autophagic flux, evident by a high LC3BII/LC3BI ratio in the presence of CQ, increased progressively with time closely mirroring the rate of decrease in mutant load (see Fig. 4B). Measurement of autophagic flux using the mCherry-GFP-LC3 probe (Fig. 6B and Fig. S7C) showed a significant increase in the formation of autolysosomes (red puncta) as early as 24 h of drug treatment and increased upon long-term treatment in patient fibroblasts. Moreover, the ratio of green/red signal as well as the average puncta size decreased significantly, suggesting the restoration of autophagy flux in the m.3243A>G mutant cells after drug treatment.

To evaluate how the increased efficacy of autophagy affects mitophagy status, immunostaining of LC3 and cytochrome c was performed in the cybrid cells (Fig. S7D). The long-term drug treatment with RP and LY dramatically increased the association between mitochondria and autophagosomes, suggesting the restoration of mitophagy flux. To quantify mitochondrial degradation, we transfected the cells with mitochondrial-targeted mKeima (mt-Keima, Addgene plasmid #56018), which undergoes a spectral shift within acidic lysosomes. In control cells, the ratio of excitation (F_{543}/F_{458}) was high, demonstrating a differential distribution of intact (green) and degraded (red) mitochondria (Fig. S7E), while in untreated patient fibroblasts, the fragmented mitochondrial network was evident, and the proportion of high ratio (F_{543}/F_{458}) signal area to the total mitochondrial area was significantly decreased, consistent with impaired mitophagic flux (Fig. 6C). However, after 24 h of drug treatments, the (F_{543}/F_{458}) ratio increased with a concomitant increase in red puncta (degraded mitochondria) in drug-treated patient fibroblasts. Altogether, these findings confirm that inhibition of PI3K-Akt-mTORC1 signalling restores autophagy and promotes mitophagic flux in the m.3243A>G mutant cells

The progressive decrease in mutant load and increase in autophagic flux with time following PI3K-Akt-mTORC1 inhibition in the m.3243A>G mutant cells strengthened the idea that upregulated mitophagic flux drives selection against the mutant mtDNA and decreases the mutant load. To explore this further, we quantified mitophagy in patient fibroblasts expressing mtKeima, cotreated with CQ in combination with RP or LY. The cotreatment with CQ decreased the high ratio (F_{543}/F_{458}) signal to levels comparable to untreated patient fibroblasts, indicating that the CQ treatment reversed the effect of LY and RP on mitophagy (Fig. 6C). Remarkably, CQ treatment over 6 weeks in the patient fibroblasts and cybrid cells also prevented the decrease of mutant load by PI3K-Akt-mTORC1 inhibition (Fig. 6D-E), strongly

suggesting that increased mitophagy is necessary to reduce the burden of mutant mtDNA. This also argues strongly that the reduction in mutant load must be a cell-autonomous effect and cannot be attributed to the selective growth of subpopulations of the cells. Together, effective autophagy/mitophagy triggered by inhibition of the PI3K-Akt-mTORC1 axis is necessary to eliminate the mutant m.3243A>G mtDNA.

DISCUSSION

The clinical presentation of disease caused by pathogenic mtDNA mutations is highly heterogeneous[4–6]. The association between specific mtDNA mutations, heteroplasmic mutant load, disease manifestation and severity are poorly understood. In the present study, we have systematically characterised the metabolic and cell signalling phenotype of cells bearing the m.3243A>G mutation, the most prevalent mtDNA mutation which is responsible for mitochondrial encephalomyopathy, lactic acidosis and stroke-like episodes (MELAS) or Maternally inherited Diabetes and Deafness (MIDD) and related disorders. We found that the changes in metabolism were associated with the constitutive hyperactivation of the PI3K-Akt-mTORC1 pathway specifically associated with the m.3243A>G mtDNA mutation. Most notably, pharmacological inhibition of PI3K, Akt, or mTORC1 in the patient-derived cells reduced mutant load and rescued mitochondrial bioenergetic function. These inhibitors promoted the upregulation of mitophagy, which was absolutely required to mediate the effects of these treatments (Fig. 6F). In contrast to the m.3243A>G mtDNA variant, previous studies have reported downregulation of Akt activity in cells carrying the m.8993T>G mutation[35], in which inhibition of the PI3K-Akt-mTORC1 pathway had no impact on mutant load or mitochondrial function (Fig. S5J). These findings suggest that the changes in signalling pathways are disease specific and may represent a link between genotype and phenotype.

Metabolic features of the patient fibroblasts and cybrid cells are consistent with most of the previous studies of the m.3243A>G mutation, including mitochondrial dysfunction, upregulated glycolysis, increased ROS production, and redox imbalance[5,15,19,30,32,36]. However, metabolic profiling of cells bearing the mutation is limited in the literature. Metabolomics data showed that reductive carboxylation of glutamine is a major mechanism to support cell survival and maintain redox balance in the m.8993T>G mutation cell models[27,37]. In contrast, using a similar approach, we found that glucose anabolism (i.e. upregulated upper glycolysis, PPP, and lipid synthesis) is increased in the m.3243A>G mutant cells and these cells are dependent on glucose for cell survival and proliferation. Also, increased TCA cycle entry of pyruvate through PC, which, combined with the prediction of enriched malate-aspartate shuttle pathway (Fig. 2A) may serve as a mechanism to maintain cellular NADH/NAD^+ balance to support glycolytic flux and promote antioxidant capacity[27,38]. This difference in metabolism between the m.8993T>G and m.3243A>G mutations argues that the mtDNA mutations cannot be seen as one disease[29,39]. Thus, the rewired metabolism specific to the m.3243A>G mutation drew our attention to the corresponding changes in cell signalling.

The alterations of metabolism in the m.3243A>G mutant cells strongly imply a perturbation in cell signalling, especially implicating the PI3K-Akt-mTORC1 pathway, which has been widely studied in

cancer signalling and metabolism[40]. For example, oxidative stress and redox imbalance may activate PI3K-Akt, the increased glycolytic flux and PPP implies an activated Akt-NRF2 signalling, the increased PC expression and p-PDH suggests an accumulation of acetyl-CoA associated with Akt-mTORC1 activity, and the accumulation of cholesteryl ester can result from excessive lysosomal free cholesterol, which also activates mTORC1[40,41]. Metabolic pathway analysis using RNA-seq data recapitulated these metabolic changes in the patient fibroblasts. Moreover, network analysis using the RNA-seq data further validated the link between the metabolic changes and altered cell signalling in cells carrying the m.3243A>G mutation. In addition, defective autophagy, because of chronic activation of the PI3K-Akt-mTORC1 pathway, may impair the selective degradation of lipid droplets (lipophagy) and contribute to the accumulation of lipid droplets in the m.3243A>G mutant cells. Sphingomyelin accumulation, as one of the features of the lipidomic data, may damage lysosomes, also contributing to impaired autophagy[13,42].

Although the mechanisms of crosstalk between PI3K-Akt-mTORC1 and EIF2 pathways are still unclear, these two pathways seem to communicate and determine cell fate under stress[23,31]. Of note, the ISR/UPR^{mt} mediated by the EIF2 signalling was also downregulated by pharmacological inhibition of the PI3K-Akt-mTORC1 axis in the mutant cells. Given that the UPR^{mt} maintains mutant mtDNA in a *C. elegans* mtDNA disease model[43] and recent studies reported that OMA1 is responsible for eIF2α phosphorylation under acute mitochondrial stress[44,45], exploring the role of ISR/UPR^{mt} in the maintenance of the m.3243A>G mutation and disease progression by suppressing eIF2α phosphorylation will be interesting. Furthermore, in a published RNA-seq data set of muscle biopsies from patients with MELAS[26], FGF21 (~48 fold) and GDF15 (~9 fold) were upregulated, matching previous findings reported from muscle tissue of 'Deletor' mice[46]. In contrast, in the present study, while we did not find changes in these two genes in the patient fibroblasts, we did find upregulation of FGF16 (~33 fold), suggesting that changes in FGF pathways in response to mitochondrial dysfunction might be tissue specific.

Previous studies have suggested that different levels of heteroplasmy of the m.3243A>G mutation in cybrid cells result in different gene expression patterns and even in discrete changes in metabolism[47,48]. Another study showed that JNK was activated by ROS in cybrid m.3243A>G cells, further reducing RXRA expression[49]. In contrast, our data did not show inhibition of the RXRA pathway and suggest that chronic activation of the PI3K-Akt-mTORC1 pathway is a general response in cells with the m.3243A>G mutation despite very different levels of mutant load. Remarkably, we found that prolonged treatment with inhibitors of each component of the PI3K-Akt-mTORC1 axis reliably and reproducibly reduced mutant burden and rescued mitochondrial function in the mutant cells. Although inhibition of the PI3K-Akt-mTORC1 axis has been shown to be beneficial in several

mitochondrial and neurological disease models, the underlying mechanisms remain elusive[13,21,50–52]. As a result, the therapeutic efficacy of the inhibition may be distinct and limited in different models. A study of a mouse model of Leigh syndrome showed that rapamycin, while delaying the progression of the disease, failed to improve OxPhos[53]. Similarly, another study showed that mTORC1 inhibition failed to improve either mitochondrial bioenergetics or survival in a mouse model of mitochondrial encephalomyopathy ($Coq9^{R239X}$)[54]. Our data from cells with the m.8993T>G mutation suggest that changes in signalling pathways may differ between mtDNA diseases, perhaps pointing towards the mechanisms that define differences in disease phenotype between different mitochondrial diseases, and emphasising that therapeutic options should be considered separately for each disease related to mtDNA mutations. However, since both the PI3K-Akt-mTORC1 axis and the accumulation of mtDNA mutations have been associated with neurodegeneration, ageing and cancers, our study may implicate in a broader biomedical context[4,6,10,21,40].

Overall, the m.3243A>G mutation causes a profound cell metabolic and signalling remodelling, although the causality between the observed alterations in metabolism and cell signalling of the m.3243A>G mutant cells is not yet conclusive. Our working model is that activation of the PI3K-Akt-mTORC1 pathway drives a metabolic rewiring of the cell, redirecting glycolytic metabolism and promoting lactate production. Activating mTORC1 suppresses mitophagy, allowing the mutation to propagate and thus maintaining the mutant load. Inhibition of the PI3K-Akt-mTORC1 axis promotes mitophagy, reduces mutant load and improves bioenergetic competence in a cell-autonomous way. Thus, we propose that nutrient-sensing pathways that may have evolved as adaptive responses to altered cellular metabolism prove to be maladaptive, driving a positive feedback cycle that may shape the phenotype of the disease and determine disease progression. In conclusion, our results suggest that activation of the PI3K-Akt-mTORC1 axis by changes in intermediary metabolism controls the heteroplasmic burden of the m.3243A>G mutation and may define disease progression and severity in a cell-autonomous manner. These data strongly suggest that cell signalling pathways activated by altered metabolism represent potential therapeutic targets that may benefit people suffering from diseases caused by mtDNA mutations.

Figure 1

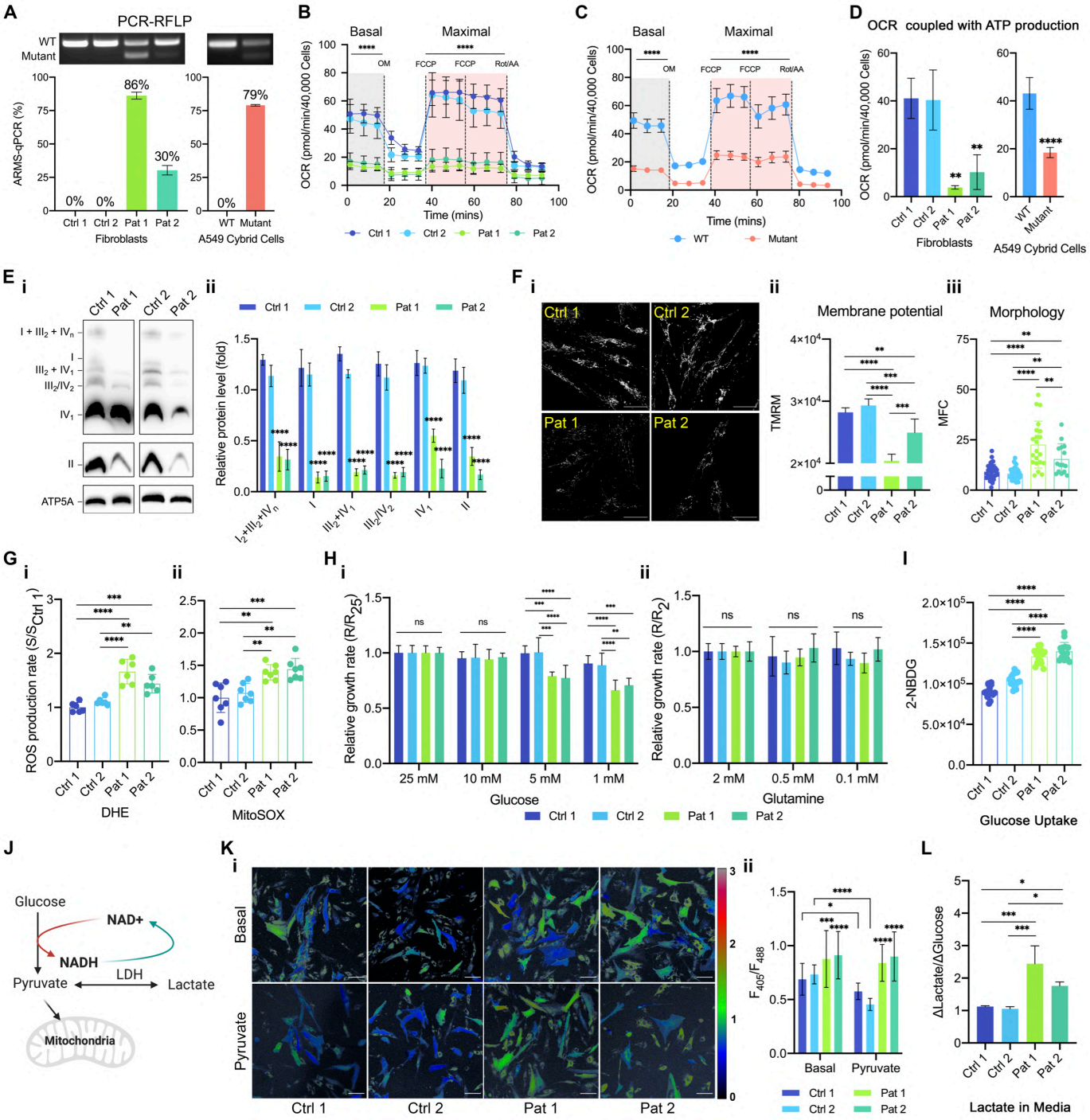

Figure S1

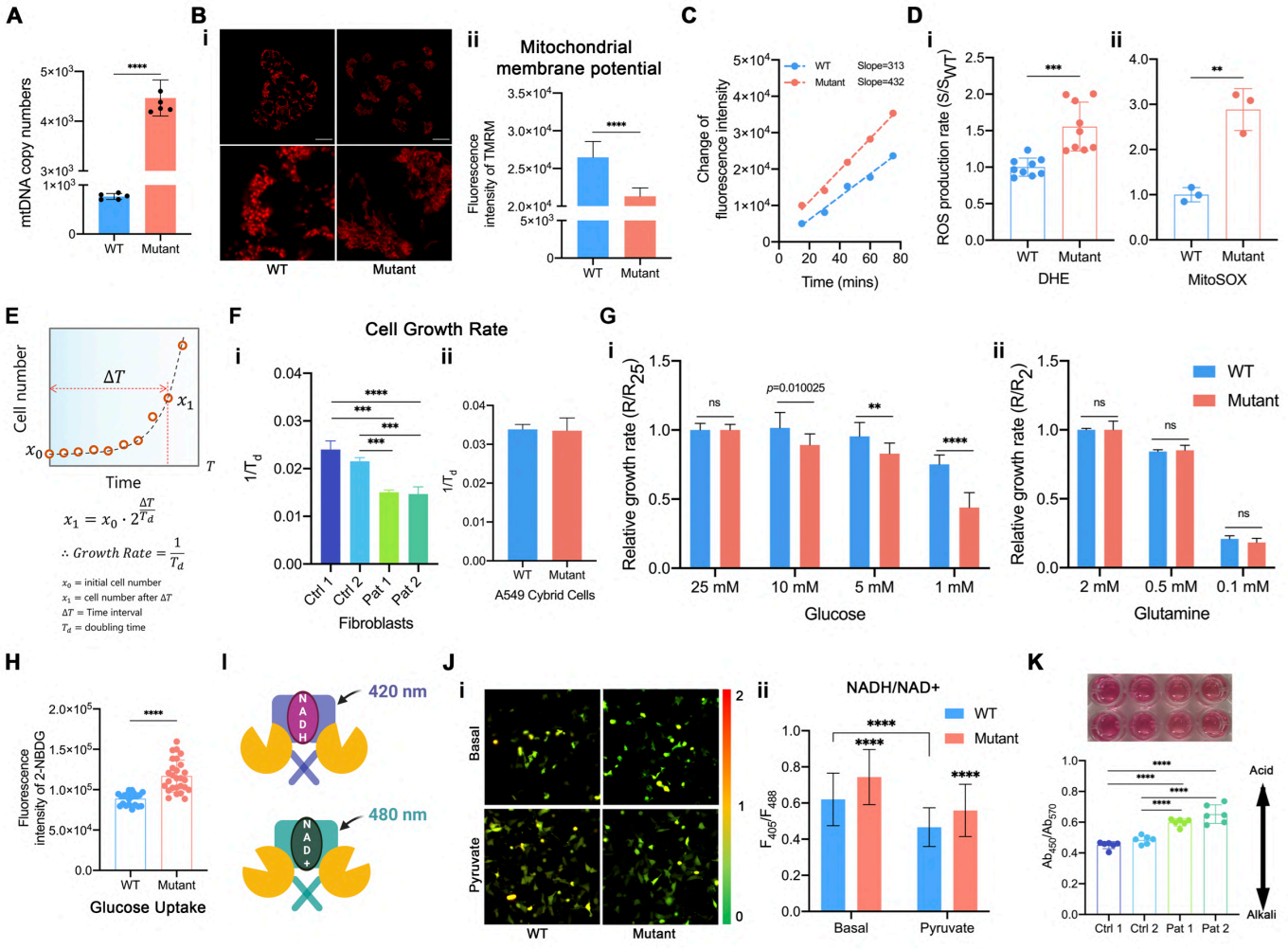

Figure 2

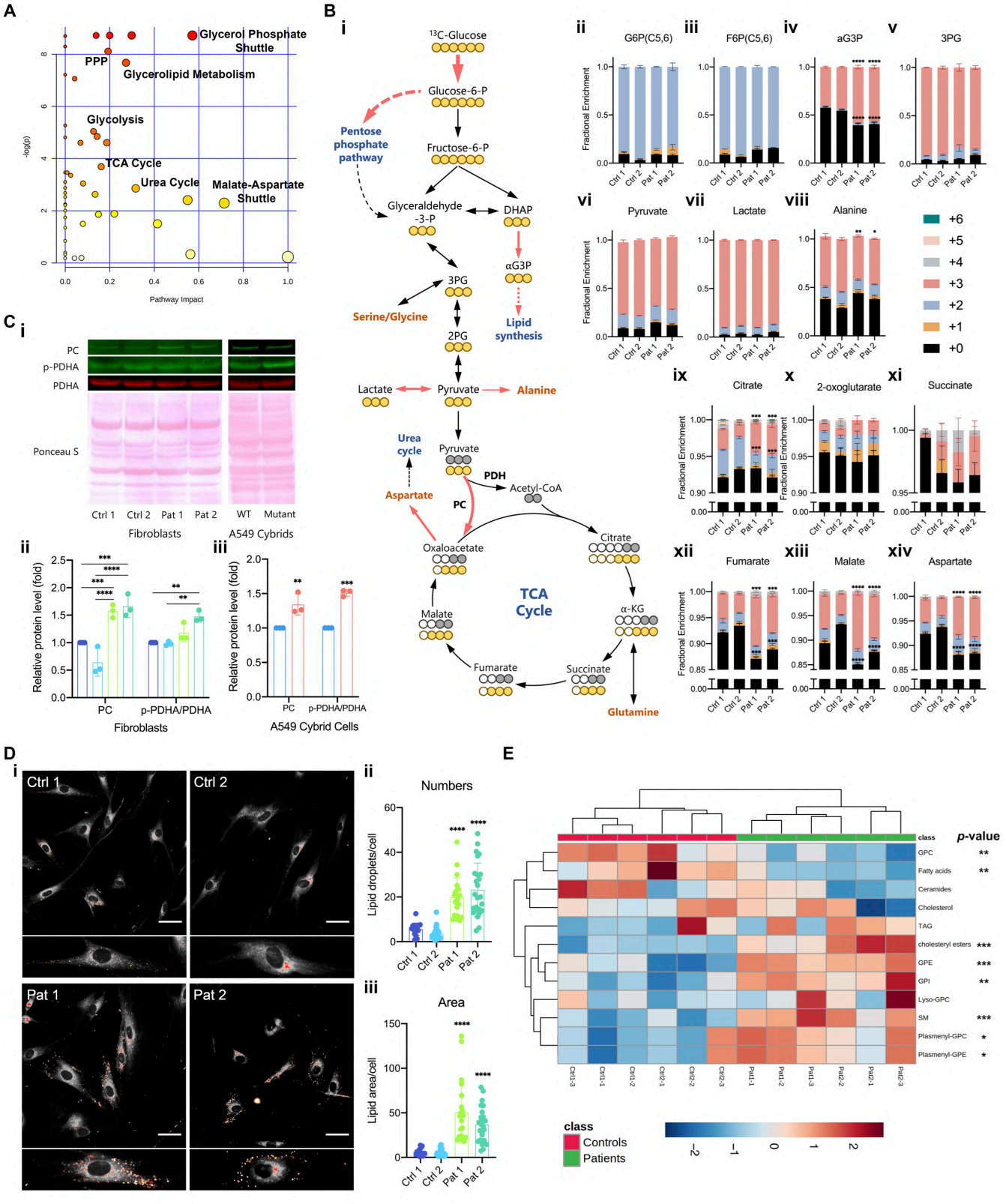

Figure S2

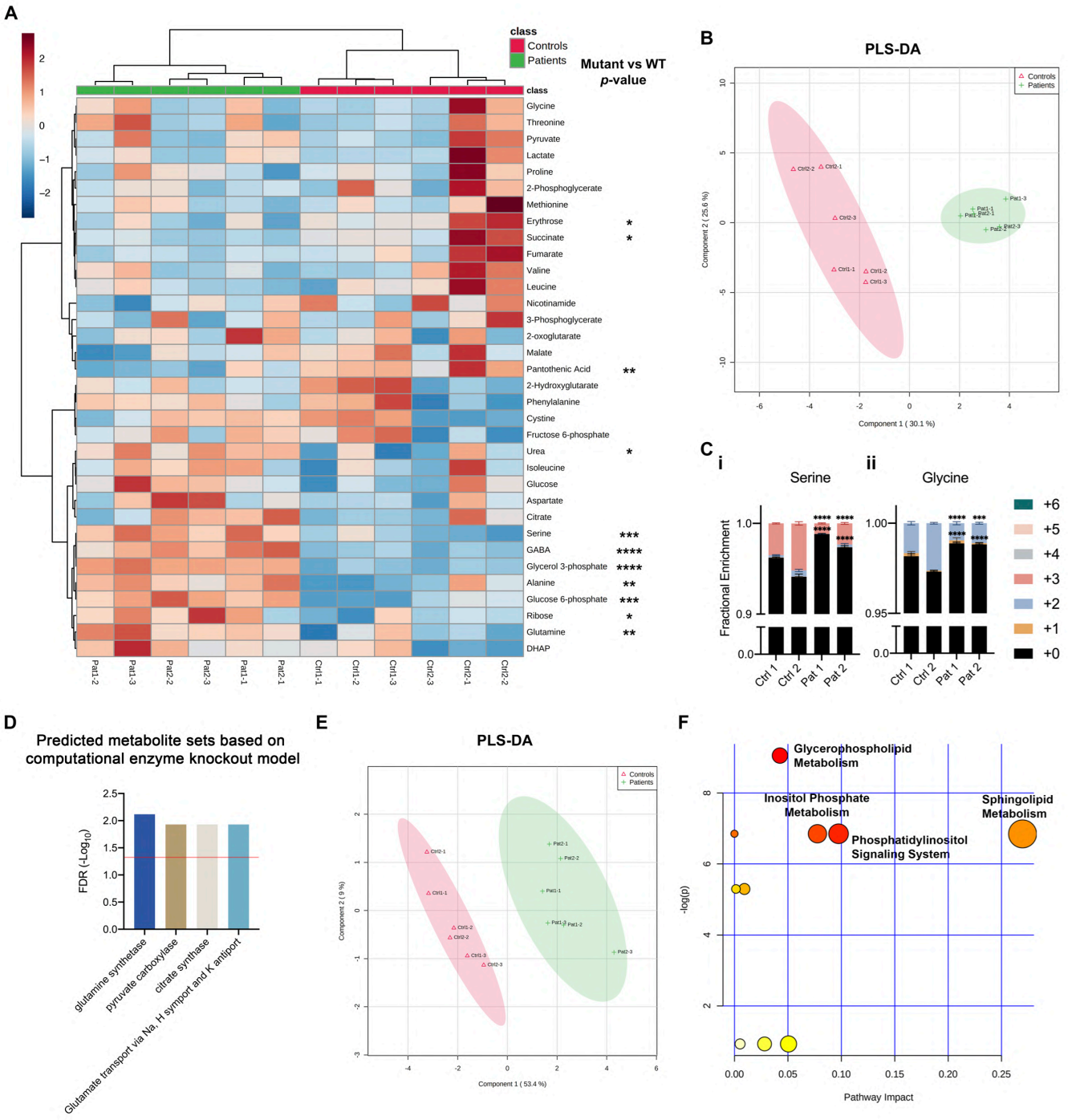

Figure 3

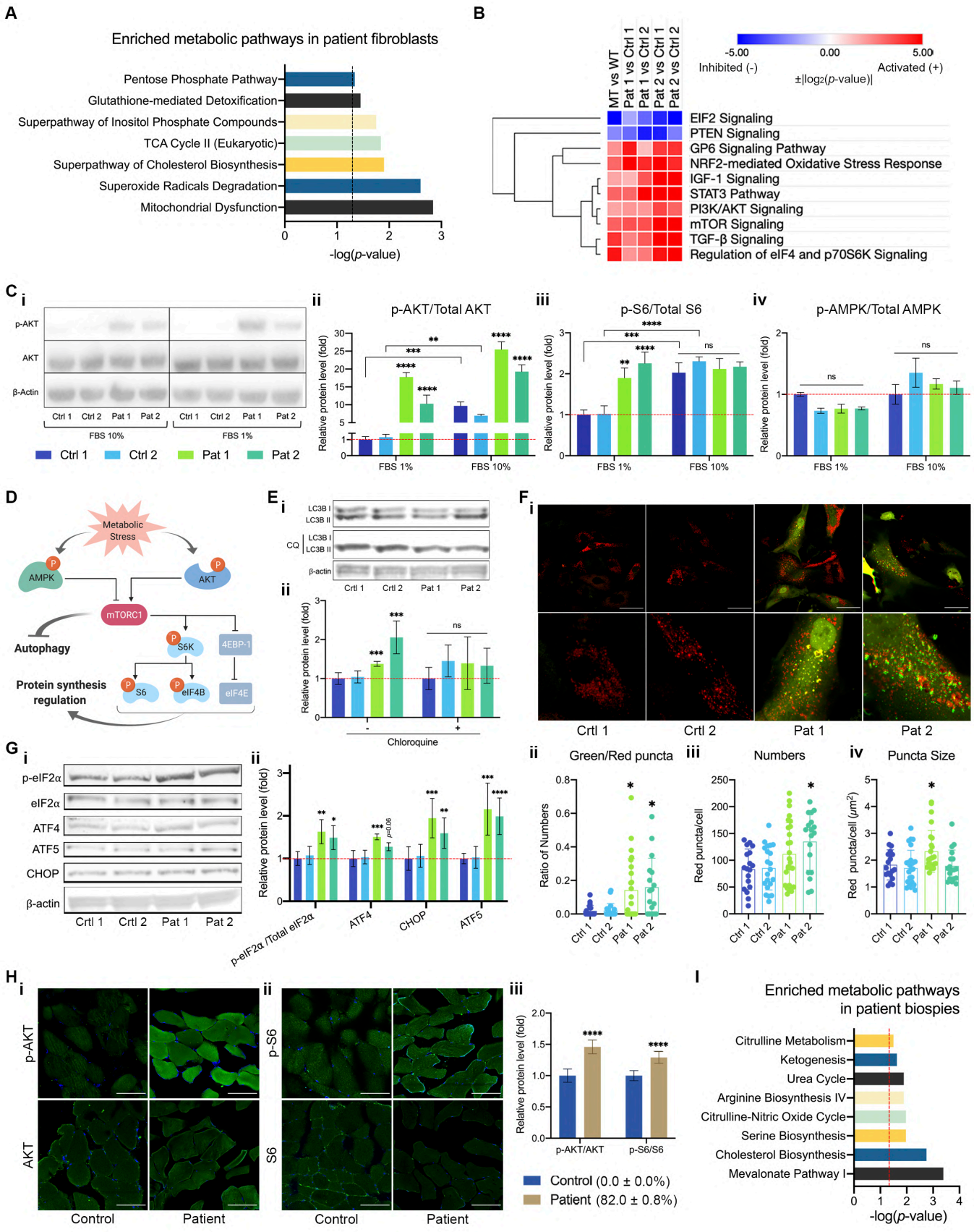

Figure S3

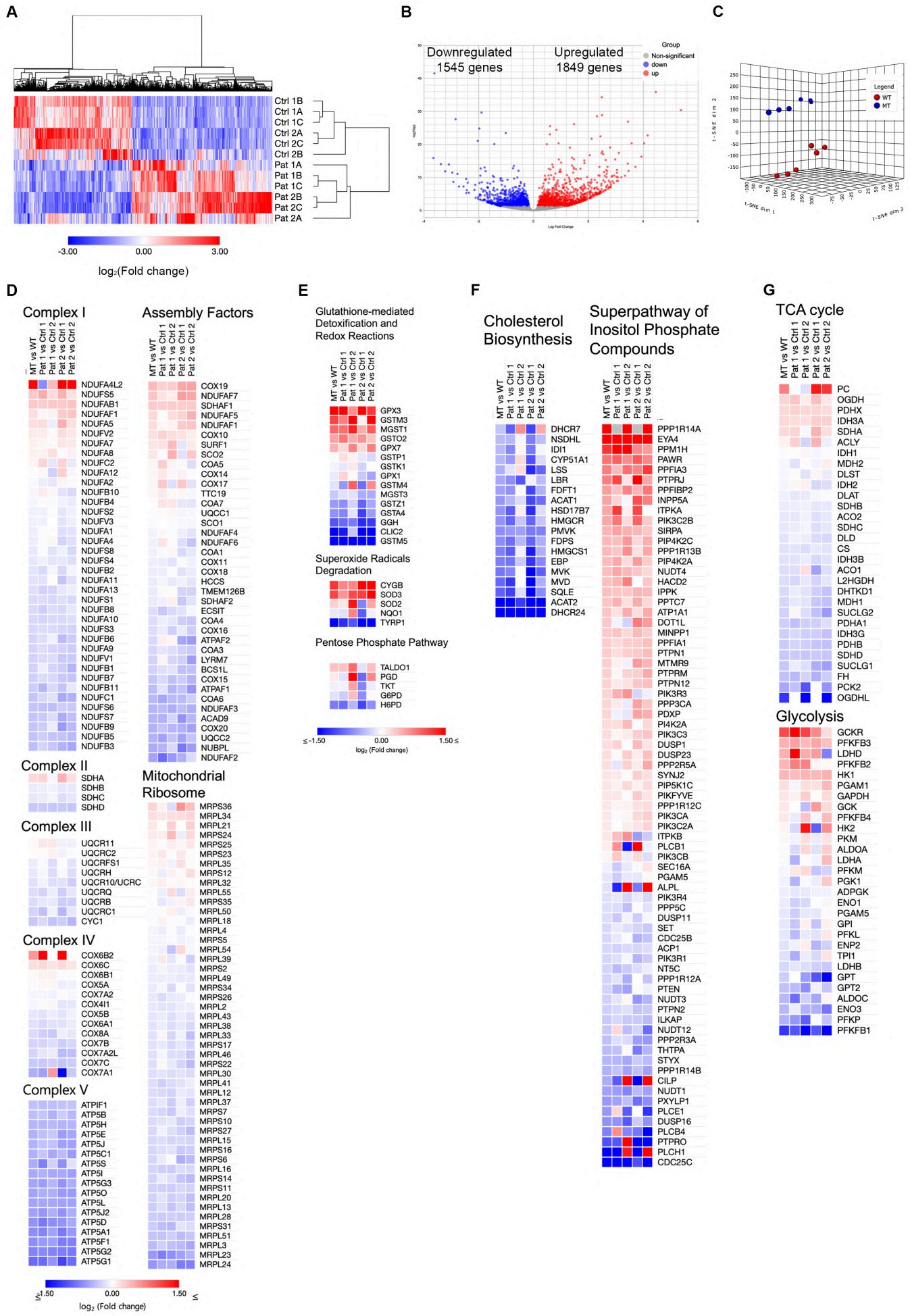

Figure S4

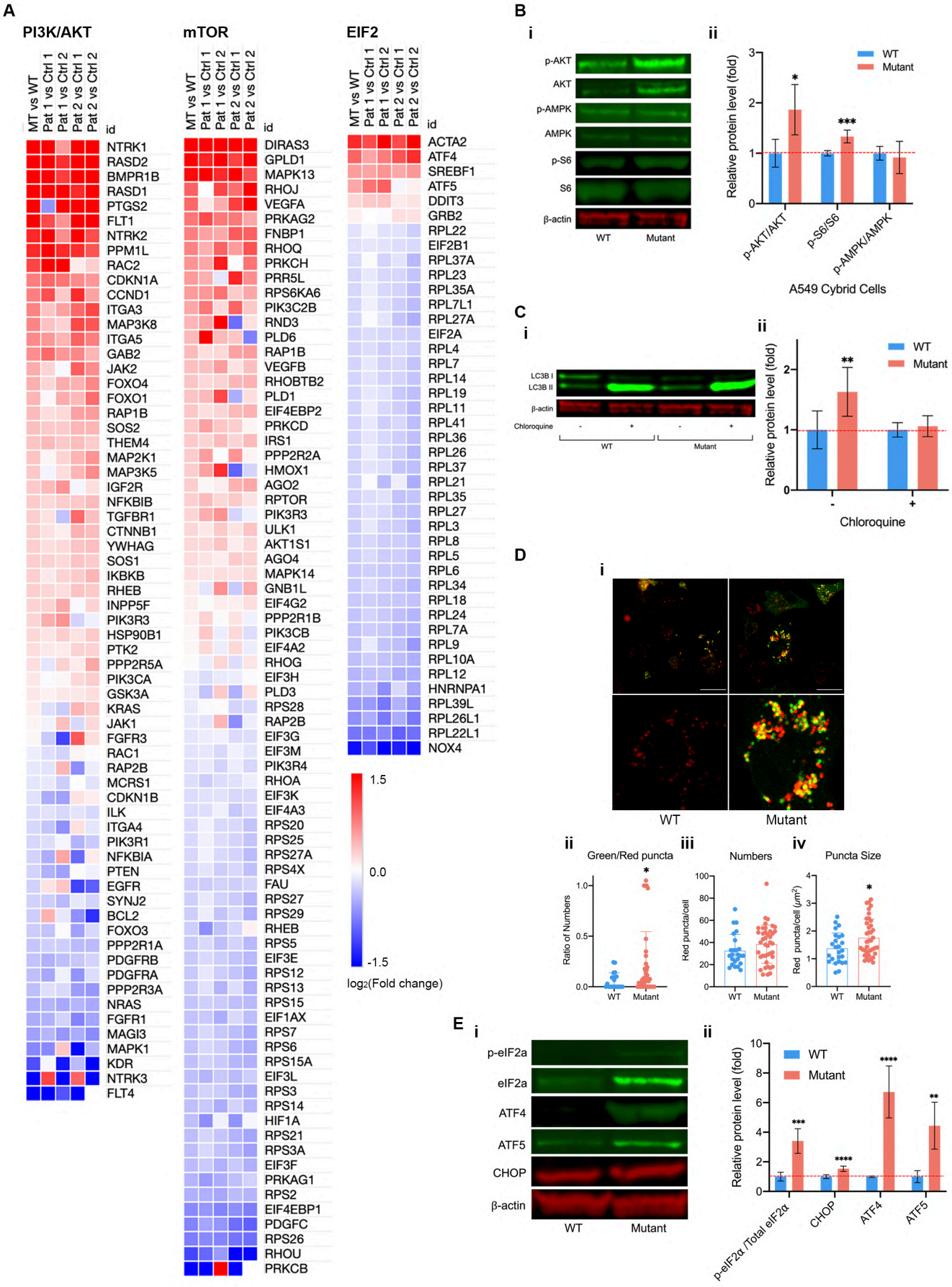

Table S1-4

Table S1. Upstream analysis for Kinase in patient fibroblasts by IPA.

Kinase	Prediction	Z-score	*p*-value
CDKN1A	Activated	3.084	1.12E-08
IKBKB		3.244	0.000377
AKT1		2.47	0.00201
MAPK13		2.079	0.00245
TGFBR2		2.747	0.00255
PTK2		2.48	0.00302
CHUK		4.427	0.00929
STK11	Inhibited	-2.494	0.00000766
INSR		-2.032	0.000675
CCNK		-2.399	0.000866
AURKB		-2.772	0.005

Table S2. Upstream analysis for translation regulator in patient fibroblasts by IPA.

Translation regulator	Prediction	Z-score	*p*-value
EIF4E	Inhibited	-2.169	0.000541
EIF4G1		-2.333	0.00245

Table S3. Upstream analysis for transcription regulators in patient fibroblasts by IPA.

Transcription regulator	Prediction	Z-score	*p*-value
TP53	Activated	3.282	2.79E-21
NUPR1		4.066	5.29E-11
KDM5B		3.627	0.00000101
CTNNB1		2.96	0.00000321
NFKBIA		2.632	0.0000157
GLI1		2.971	0.0000256
TCF4		2.225	0.0000457
SMARCA4		3.609	0.000108
KLF4		2.946	0.000627
PTTG1		2.302	0.000791
TFEB		3.273	0.0008
CDKN2A		4.62	0.000838
TCF7L2		4.059	0.000841
TCF3		3.926	0.00118
HIF1A		2.117	0.00224
CREB1		3.164	0.00238
HDAC1		2.228	0.00248
RBCK1		2.236	0.00252
E2F6		2.53	0.00259
ATF4		2.495	0.00296
SMARCD3		2.813	0.005
HDAC2		2.468	0.00621
ERG		2.557	0.00988
EP300		2.298	0.00994
TBX2	Inhibited	-4.488	2.43E-08
MYC		-4.01	2.46E-07
MYCN		-5.406	0.00000442
GMNN		-2.746	0.0000098
SOX1		-3	0.0000215
HOXA9		-2.01	0.0000273
E2F3		-3.186	0.0000273
SOX3		-3	0.00012
RUNX3		-2.272	0.000213

Table S4. Upstream analysis using published RNA-seq dataset of patient biopsies by IPA.

Upstream Regulator	Molecule Type	*p*-value
TRIB3	Kinase	0.0000295
MTOR		0.00112
TGFBR2		0.0101
GNE		0.0155
PIK3R1		0.0159
TGFBR1		0.0166
CDK19		0.0199
Growth hormone	Group	0.000165
Foxo		0.000504
ADRB		0.00393
Insulin		0.00402
YAP/TAZ		0.0089
Pro-inflammatory Cytokine		0.0101
PI3K (family)		0.026
Rxr		0.0269
ATF4	Transcription Regulator	0.00048
MLX		0.000905
PPARGC1A		0.00115
EP300		0.0029
FOXO1		0.00299
MLXIPL		0.00326
MLXIP		0.00446
ZNF282		0.0089
MYRF		0.0104
HDAC5		0.0122
NKX2-3		0.0127
MYC		0.0131
STAT6		0.0149
ZNF100		0.0155
ZNF85		0.0155
ZNF254		0.0155
ZNF431		0.0155
ZNF43		0.0155
ZNF429		0.0155
HDAC10		0.0177
ZNF91		0.0177
ATF5		0.0221
PA2G4		0.0221
KAT5		0.0231
STAT5B		0.026
AJUBA		0.0265
DDIT3		0.0282
BHLHE41		0.0287
ARNT		0.0304
PIAS4		0.0308
THRAP3		0.033
PLAGL1		0.033
KLF11		0.0337
CREBZF		0.0352
CBX4		0.0352
TCF7L2		0.0374
MNT		0.0416
ACTN4		0.0416
CREB3L3		0.0438
NONO		0.0438
MED12		0.0459
SIN3B		0.0459
PBX3		0.048
HNF4A		0.048
MED1		0.0492

Figure 4

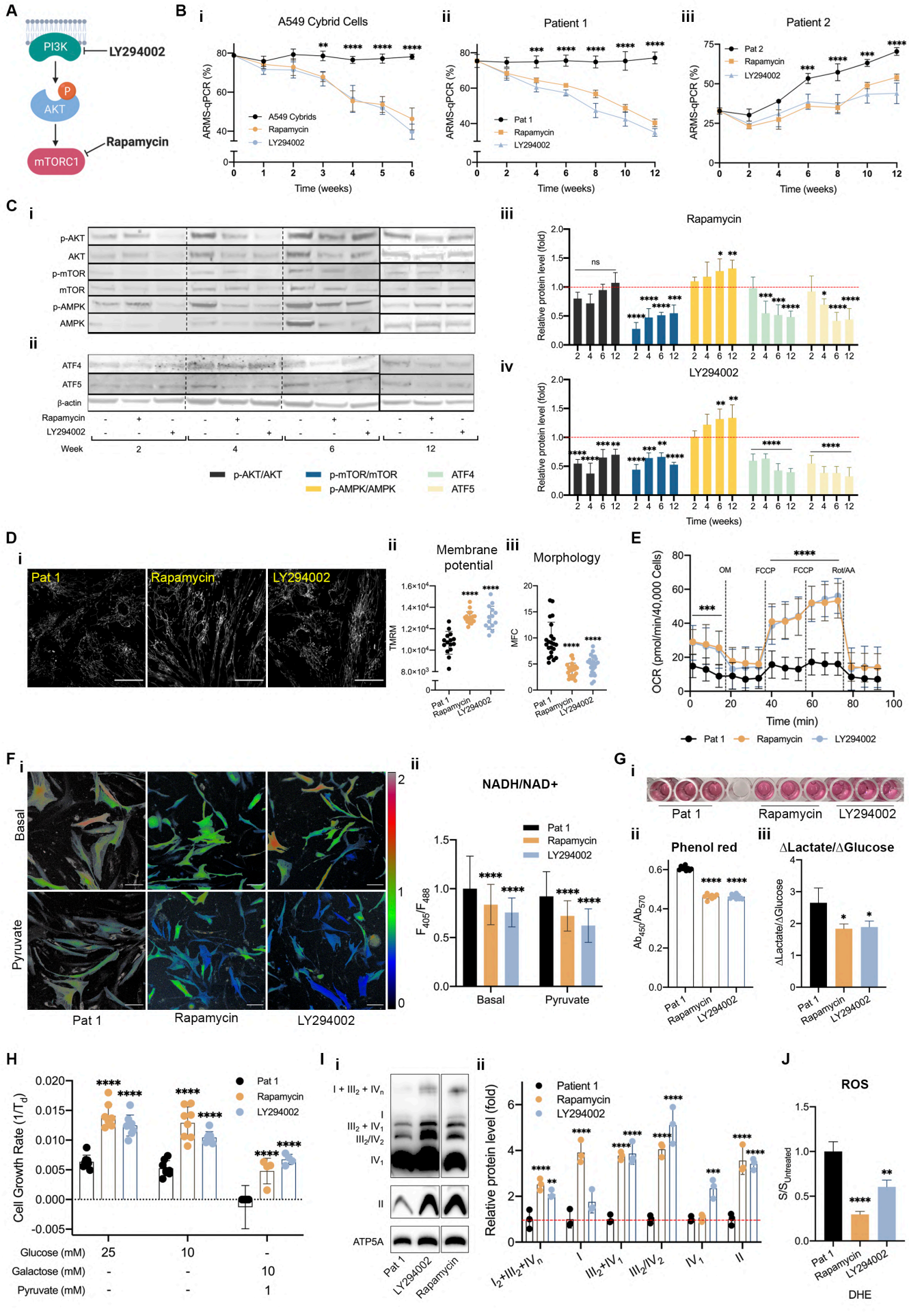

Figure S5

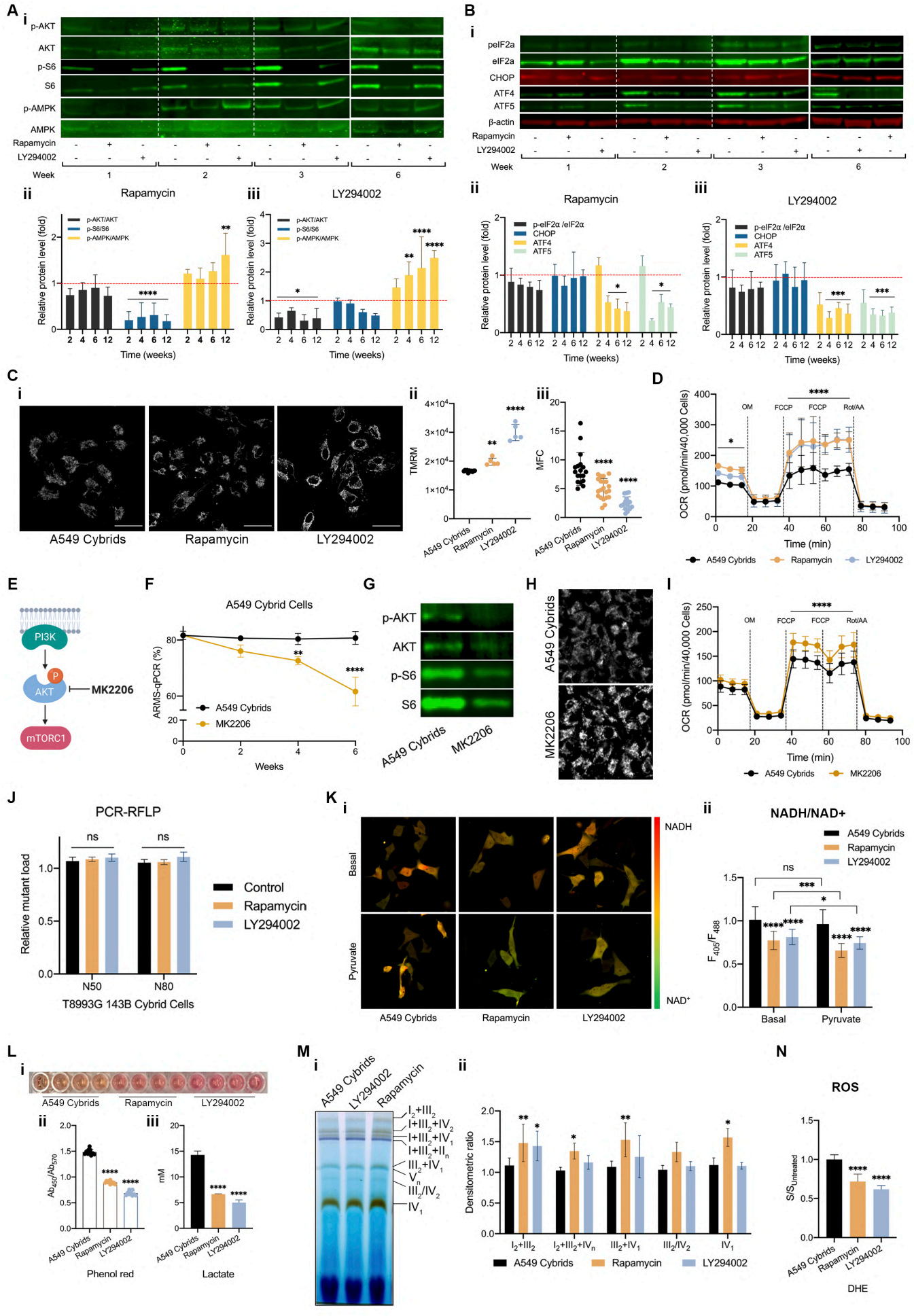

Figure 5

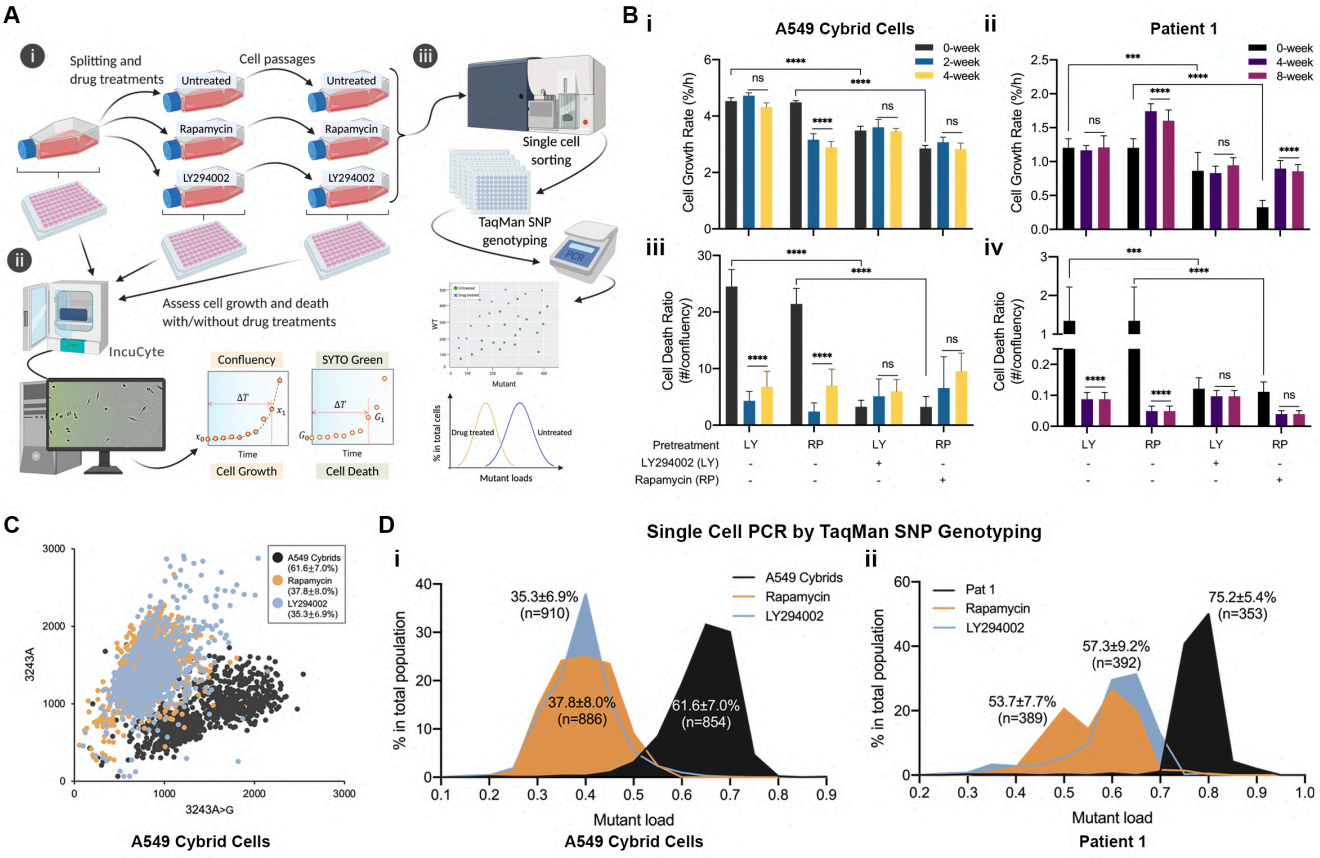

Figure S6

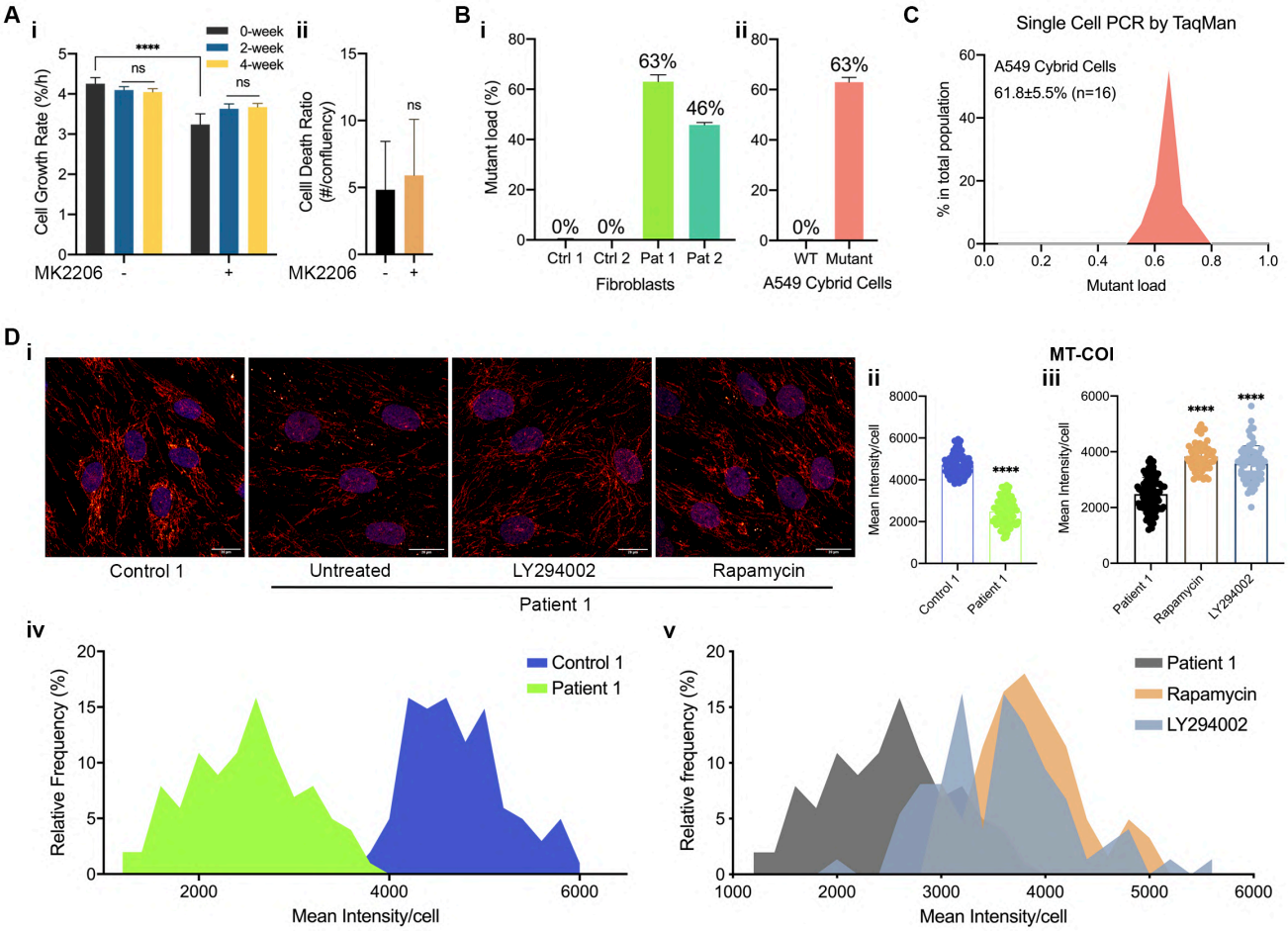

Figure 6

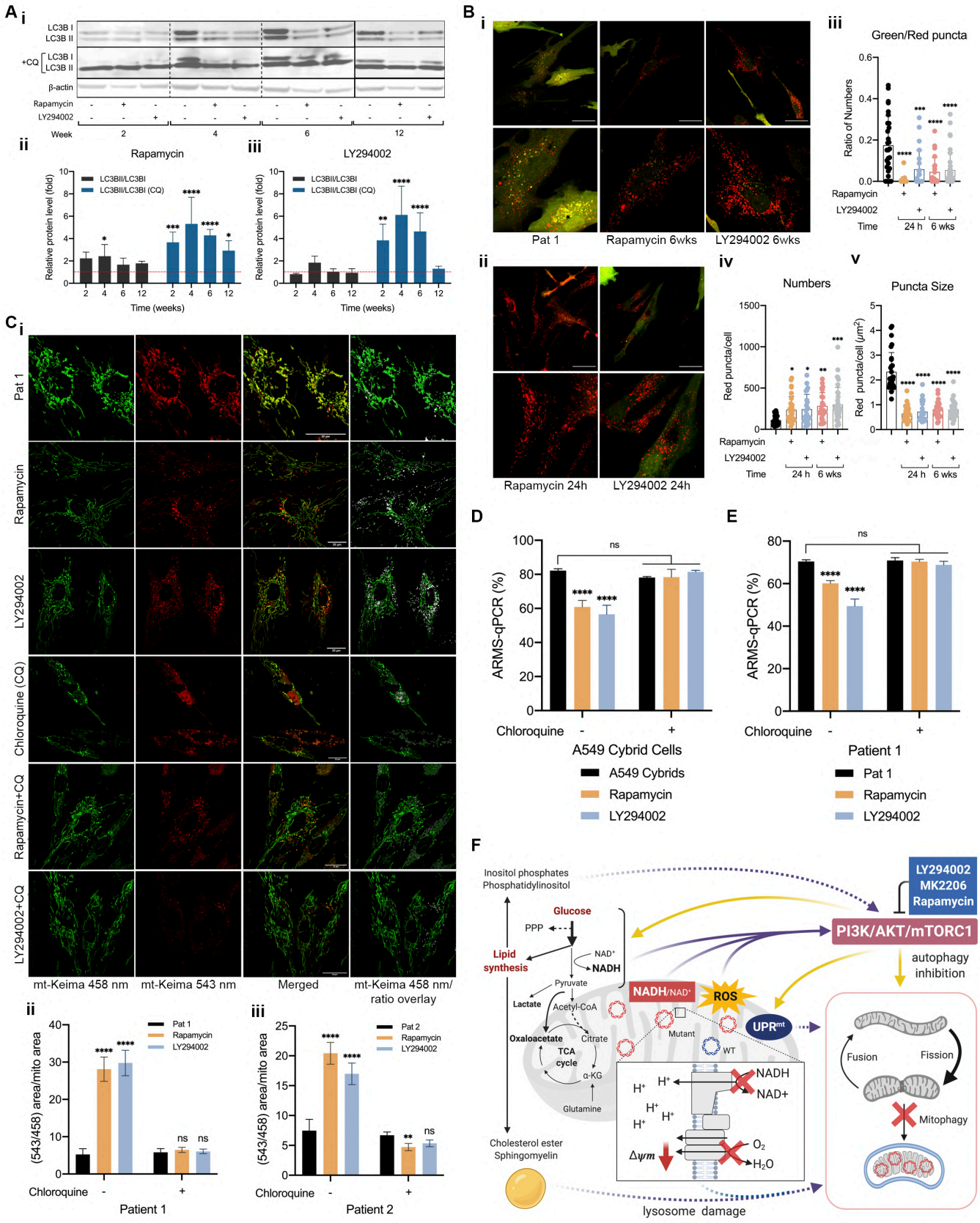

Figure S7

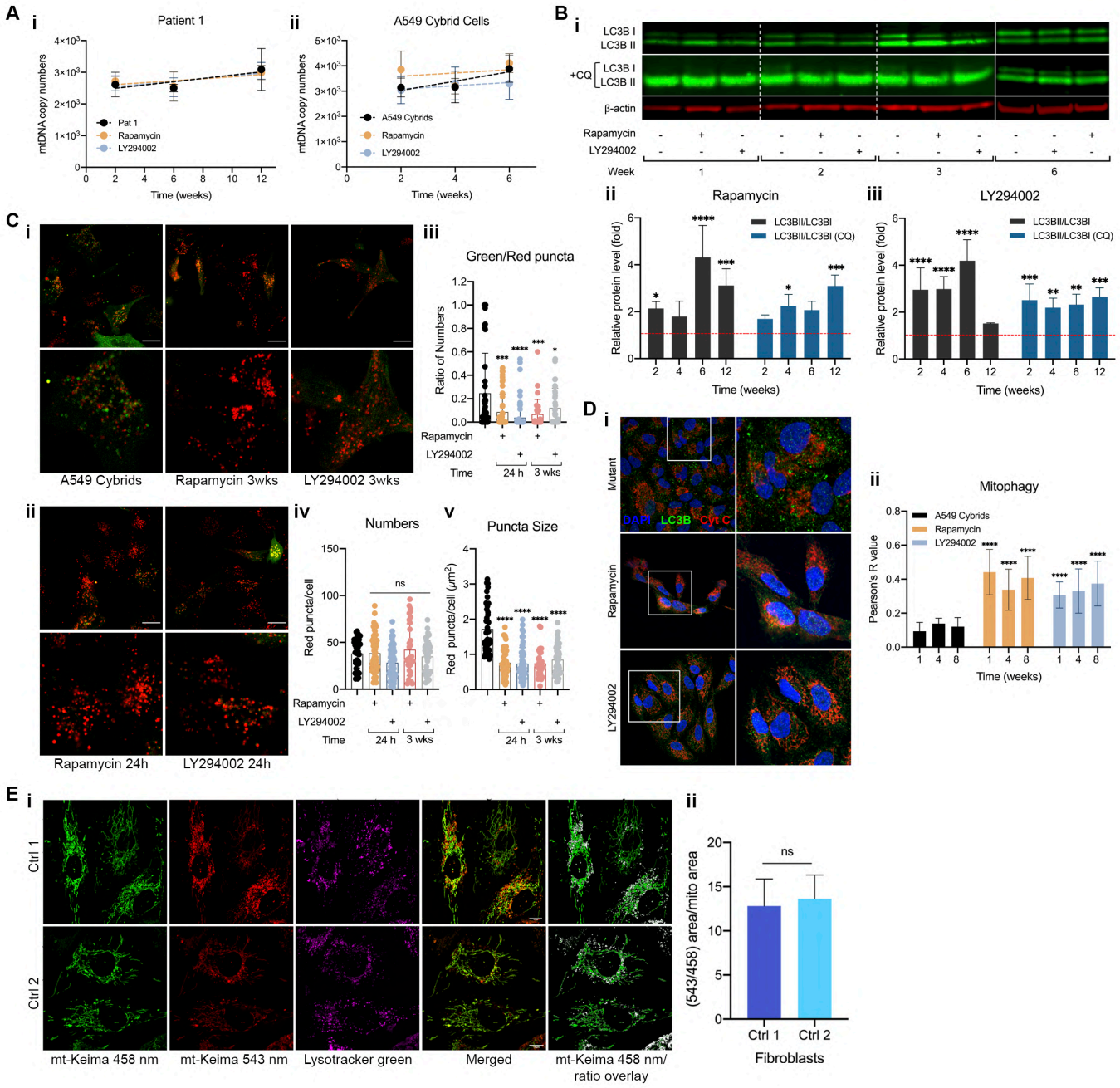

FIGURE LEGENDS

Figure 1. The m.3243A>G mtDNA mutation causes mitochondrial dysfunction and switches cell metabolism to a more glycolytic phenotype, resulting in redox imbalance and oxidative stress.

(A) PCR-RFLP and ARM-qPCR were used to quantify the mutation load for patient-derived fibroblasts (n = 3 independent biological samples) and A549 cybrid cells (n = 5 independent biological samples).

(B-D) Cell respiratory capacity was measured using the Seahorse XFe96 extracellular flux analyser in patient fibroblasts (B, n = 6 culture wells) and A549 cybrid cells (C, n = 9 culture wells, further normalised to mtDNA copy number), showing a major decrease in oxygen consumption under all conditions. (D) oxygen consumption dependent on ATP production– the response to oligomycin – is plotted.

(E) The expression of respiratory chain proteins and supercomplex assembly in patient fibroblasts assessed using blue native gels electrophoresis (BNGE, i) and quantified (ii), showing a major decrease in the assembly of all supercomplexes from the patient-derived cells (n = 3 independent experiments)

(F) The mitochondrial membrane potential of fibroblasts was measured using TMRM with confocal microscopy (i) and quantified (ii), showing a significant decrease in potential (n = 5 independent experiments). The images were further analysed using the mitochondrial fragmentation count (MFC) for mitochondrial morphology (iii), confirming the impression of a fragmented phenotype (n=25 cells). Scale bar = 50 μm.

(G) ROS production rates of patient fibroblasts were measured using the reporters, DHE (i) and MitoSOX (ii). Rates of production were significantly increased in patient-derived cells (n = 6 independent biological samples).

(H) The growth rates of patient fibroblasts were measured under a range of different nutrient conditions (normalised to the growth rate of each cell line in regular cell media), showing a decrease of growth rate compared to controls at glucose concentrations of 5 and 1 mM (i) but not at low glutamine (ii) concentrations (n = 6 culture wells for all conditions, 3 independent experiments).

(I) Glucose uptake in patient fibroblasts was measured using the fluorescent glucose analogue, 2-NBDG, showing a significantly increased rate of glucose uptake in the patient fibroblasts (n = 15 culture wells).

(J) Schematic depicting the simplified mechanism that maintains cytosolic NADH:NAD^+ balance.

(K) NADH:NAD^+ ratio of fibroblasts was measured using the reporter, SoNar, under basal conditions and after addition of pyruvate (200 μM, 30 min; i) and quantified (ii; n = 50±10 cells). Scale bar=100 μm.

(L) Lactate production (normalized to glucose consumption) was measured in the media of fibroblasts using CuBiAn and showed a significant increase in lactate release in the media of patient-derived cells (n = 4 independent biological samples).

All data are represented as mean ± s.d. and data were analysed by one/two-way ANOVA with Tukey's multiple comparisons test for fibroblasts and by unpaired t test for cybrid cells (* $p < 0.05$, ** $p < 0.01$, *** $p < 0.001$, **** $p < 0.0001$).

Figure S1. The metabolic phenotype of A549 cybrid cells recapitulates the metabolic features of patient fibroblasts.

(A) Mitochondrial DNA copy number (ii, n = 5 independent biological samples) of A549 cybrid cells.

(B) The mitochondrial membrane potential of A549 cybrid cells measured using TMRM with confocal imaging (scale bar=20 μm, n = 7 independent biological samples).

(C-D) Rates of ROS production in A549 cybrid cells and the parental cells were measured using dihydroethidium (DHE), as the rate of increase in red fluorescence intensity over 80 min incubation with DHE. (D) ROS production rates of A549 cybrid cells reported by DHE (i, n = 9 independent biological samples) and MitoSOX (ii, n = 3 independent biological samples).

(E-G) A scheme describing how growth rates were obtained by fitting growth curves with an exponential cell growth model (E). Based on the model, growth rate of fibroblasts (n = 3 culture wells) and A549 cybrid cells cultured with regular medium were obtained (n = 5 culture wells, $p = 0.84$; F). (G) Cell growth rates of A549 cybrid cells were measured under a range of different nutrient conditions (normalised to the growth rate of each cell line in regular cell media), showing a decreased rate of growth of A549 cybrid cells compared to controls at glucose concentrations of 5 and 1 mM (i; n = 10 culture wells) but not at low glutamine (ii) concentrations (n = 6 culture wells).

(H) Glucose uptake in A549 cybrid cells was measured by 2-NBDG, showing a significantly increased rate of glucose uptake in the cybrid cells compared to A549 controls (n=21 culture wells).

(I) Schematic depicting the ratiometric probe for NADH:NAD^+, SoNar.

(J) NADH:NAD^+ ratio of A549 cybrid cells under basal condition and after addition of pyruvate (200 μM, 30 min; i) was measured by the probe and quantified (ii; n = 180 cells).

(K) pH in the media from patient fibroblasts cultured for 2 days was measured based on the ratiometric property of the pH indicator in media, phenol red, and showing a lower pH in the media of patient fibroblasts than that of controls (n = 6 independent biological samples).

All data are represented as mean ± s.d. and were analysed by one/two-way ANOVA with Tukey's multiple comparisons test for fibroblasts and by unpaired t test for cybrid cells (* $p < 0.05$, ** $p < 0.01$, *** $p < 0.001$, **** $p < 0.0001$).

Figure 2. The m.3243A>G mutation rewires glucose and lipid metabolism towards increased anabolic biosynthesis and lipid accumulation.

(A) The concentration of metabolites obtained by GC-MS was used to determine the enriched metabolic pathways in patient fibroblasts by MetaboAnalyst 4.0., suggesting that phospholipid biosynthesis, PPP, glycolysis, TCA cycle, etc. were enriched (n = 6 technical replicates.).

(B) Schematic of simplified glucose metabolism of the cells (i) Red arrows, upregulated pathways or reactions; three yellow circles of pyruvate and beyond, pyruvate is converted to OAA by pyruvate carboxylase; three or two grey circles of pyruvate and beyond, pyruvate is converted to acetyl-CoA by PDH. Tracing the distribution and abundance of ^{13}C enrichment in the intermediates of glycolysis (ii-viii) and the TCA cycle (ix-xiv) combined with Fig S2A revealed an increase in lipid synthesis and PC activity (n = 4 independent biological samples).

(C) Immunoblotting (i) of the expression of pyruvate carboxylase and phosphorylation state of PDH showed an increase of pyruvate carboxylase expression and increased phosphorylation of PDH (which reduces its activity) in patient fibroblasts (ii) and A549 cybrid cells (iii) (n = 3 independent experiments for all cell lines).

(D) Nile Red O staining (i) showing the numbers (ii) and area (iii) of lipid droplets in patient fibroblast (n = 20 cells). Scale bar = 50 μm.

(E) Lipid profiles of patient fibroblasts acquired by LC-MS were analysed by MetaboAnalyst 4.0., showing a strikingly increased content of Inositol phosphate, cholesterol esters and sphingomyelin (n = 6 independent biological samples). GPC, glycerophosphatidylcholines. TAG, triacylglycerols. GPE, glycerophosphatidylethanolamines. GPI, glycerophosphatidylinositols. SM, sphingomyelins.

All data, except Figs. 2A and 2E, are represented as mean ± s.d. and were analysed by one/two-way ANOVA with Tukey's multiple comparisons test for fibroblasts and by unpaired t test for cybrid cells (* $p < 0.05$, ** $p < 0.01$, *** $p < 0.001$, **** $p < 0.0001$).

Figure S2. The metabolomic and lipidomic profiles of fibroblasts carrying the m.3243A>G mutation are distinct from that of their matched controls.

(A) The heatmap of metabolite concentrations obtained by GC-MS was generated by MetaboAnalyst 4.0 (n = 3 technical replicates), revealing significant differences in the concentrations of several metabolites between controls and patient fibroblasts.

(B) PLS-DA for the dataset of Fig. S2A showed that the metabolic profiles of patient fibroblasts were distinct from that of controls.

(C) A reduced incorporation of ^{13}C into serine (i) and glycine (ii) and an increase of serine concentration (Fig S2A) in the patient cells (mean ± s.d, of n = 4 independent biological samples).

(D) Metabolite set enrichment analysis based on computational enzyme knockout model predicted that pyruvate carboxylase was affected ($p < 0.05$).

(E-F) PLS-DA (E) and enriched metabolic pathways (F) for the dataset of Fig. 2E.

All data were analysed as stated above (* $p < 0.05$, ** $p < 0.01$, *** $p < 0.001$, **** $p < 0.0001$)

Figure 3. The PI3K-Akt-mTORC1 axis is upregulated in the m.3243A>G mutant cells, prompting ISR/UPR^{mt} response and perturbing autophagy.

(A) Analysis of RNA-seq data from the patient fibroblasts by QIAGEN Ingenuity Pathway Analysis (IPA) showed the enriched metabolic pathways ($p < 0.05$), matching the findings shown in Figs. 1 and 2.

(B) RNA-seq of patient fibroblasts analysed by IPA showed cell signalling pathways which are enriched in cells carrying the m.3243A>G mutation. These include striking and significant increases in expression of pathways involving PI3K-Akt, mTOR, EIF2, and NRF2. It is notable also that PTEN expression, a negative regulator of PI3K-Akt-mTOR signalling was downregulated ($p < 0.05$, Z-score > 1; Blue, inhibited; Red, activated).

(C) Immunoblotting of p-Akt/Akt (i-ii), p-S6/S6 (iii) and p-AMPK/AMPK (iv) in patient fibroblasts grown in the presence of 10% or 1% FBS media, showing a major increase in p-Akt/Akt and p-S6/S6 in the presence of 1% FBS media in the mutant cells (mean ± s.d. of n = 3 independent experiments).

(D) A simple scheme showing the regulation of autophagy and protein translation by the PI3K-Akt-mTORC1 pathway.

(E) Immunoblotting of LC3B with chloroquine (CQ, 50 μM for 5 h; n = 4 independent biological samples) or without CQ (n = 7 independent biological samples) in patient fibroblasts (i) and quantified in (ii) suggests an accumulation of LC3BII in the patient cells without an increase in autophagic flux.

(F) confocal imaging of live cells transfected with the autophagy reporter, mCherry-GFP-LC3 in patient fibroblasts (i, n=20 cells). The ratio of green/red puncta (ii), autophagosome numbers (iii) and puncta size (iv) were further quantified, showing an increase of these indices. Scale bar = 50 μm.

(G) Immunoblotting of p-eIF2α/eIF2α, ATF4, ATF5 and CHOP in patient fibroblasts (i) showed an increase of expression or phosphorylation of these proteins (ii) (n = 3-8 independent experiment).

(H) Immunofluorescence staining for p-AKT/AKT (i, n > 60 muscle fibres) and p-S6/s6 (ii, n > 25 muscle fibres) in patient muscle biopsies confirmed the increased phosphorylation of Akt and S6 in the patients (iii). The mutant loads of the m.3243A>G mutation in biopsies were quantified by ARMS-qPCR. Scale bar = 100 μm.

(I) Re-analysis of a published RNA-seq data set of patient biopsies collected by Deng *et al.* using IPA confirmed the enrichment of metabolic pathways identified in patient-derived fibroblasts ($p < 0.05$).

All data, except Figs. 3A-B and 3I, are represented as mean ± s.d. and were analysed by one/two-way ANOVA with Tukey's multiple comparisons test for fibroblasts and by unpaired t test for biopsies (* $p < 0.05$, ** $p < 0.01$, *** $p < 0.001$, **** $p < 0.0001$).

Figure S3. Analysis for RNA-seq of patient fibroblasts and the enriched metabolic pathways recapitulates the metabolic phenotype of patient fibroblasts.

(A-C) RNA-seq showed by a heatmap (A), a volcano plot (B) and 3D-PCA (C). Gene expression in the mutant cells was significantly distinct from both of the controls: 3394 genes were differentially expressed (FDR < 0.05, with 1849 up-regulated and 1545 down-regulated)

(D) Analysis of the RNA seq data showing a general decrease in mRNA expression of OxPhos-related genes in patient fibroblasts.

(E-F) Analysis of the RNA-seq data showing an altered mRNA expression in antioxidant defence-related genes (E), a reduced mRNA expression of genes involving in the cholesterol synthesis and an altered inositol phosphate metabolism in patient fibroblasts (F).

(G) The mRNA expression of TCA cycle and glycolysis genes in patient fibroblasts confirmed our findings in Fig 2, such as increased pyruvate carboxylase and HK1 expression.

Figure S4. RNA-seq details of patient fibroblasts and supporting results from A549 cybrid cells.

(A) Detailed analysis of the mRNA expression of multiple genes involved in the PI3K-Akt, mTOR and EIF2 pathways in patient fibroblasts, showing consistent differences in a wide array of genes involved in these pathways.

(B) Immunoblotting of p-Akt/Akt, p-S6/S6 and p-AMPK/AMPK in A549 cybrid cells shows increased phosphorylation of Akt and S6 but not of AMPK, consistent with the results of fibroblasts (mean ± s.d. of n = 4-5 independent experiments, two-way ANOVA with Tukey's multiple comparisons test).

(C) Immunoblotting of LC3B with CQ (50 µM for 5 h; n = 4 independent biological samples) or without CQ (n = 10 independent biological samples) in A549 cybrid cells (ii) suggests an accumulation of LC3BII without an increase in autophagic flux (iii) as seen in the patient fibroblasts (mean ± s.d., two-way ANOVA with Tukey's multiple comparisons test)

(D) Imaging of mCherry-GFP-LC3 (n>20 cells) in A549 cybrid cells (i). The ratio of green/red puncta (ii, p = 0.0375), autophagosome numbers (iii, p = 0.1640) and puncta size (iv, p = 0.0219) were further quantified, showing an increase of green/red puncta and puncta size in the patient cells (mean ± s.d., unpaired t test for all analyses). Scale bar = 30 µm.

(E) Immunoblotting of p-eIF2α/eIF2α, ATF4, ATF5 and CHOP in A549 cybrid cells showed increased expression of all of these proteins, consistent with the results from the patient fibroblasts (mean ± s.d. of n = 5-8 independent experiments, two-way ANOVA with Tukey's multiple comparisons test).

All data were analysed as stated above (* p<0.05, ** p<0.01, *** p<0.001, **** p<0.0001).

Figure 4. Inhibitors of PI3K, Akt, and mTORC1 reduce mutation load, rescue mitochondrial function and reduce glucose dependence.

(A-B) Schematic depicting pharmacological inhibition of the PI3k-Akt-mTORC1 pathway by rapamycin (RP) or LY290042 (LY) (A). (B) Sustained treatment of cells over 6 or 12 weeks with rapamycin (5 µM) or LY290042 (5 µM) caused a progressive decrease in mutant mtDNA load in A549 cybrid cells (i) and fibroblasts of patient 1 (ii) and suppressed the progressive increase of mutant load with time in culture seen in patient 2 fibroblasts (iii) (n = 3 independent experiments). The concentrations of RP and LY here refer to all subsequent treatments.

(C) Immunoblotting of the phosphoproteins (p-Akt/Akt, p-mTOR/mTOR and p-AMPK/AMPK; i) and ISR/UPR^{mt} proteins (ii) in patient 1 fibroblasts treated with RP (iiI) or LY (iv) over 12 weeks

demonstrated the effective inhibition of Akt or mTORC1 and an amelioration of the integrated stress response (ISR) in the drug-treated cells (n = 3-4 independent experiments).

(D) The mitochondrial membrane potential of patient 1 fibroblasts treated with LY or RP for 12 weeks were significantly increased (ii) and mitochondrial fragmentation counts (MFC, iiI) were also significantly reduced (n = 15 independent biological samples). Scale bar = 50 μm.

(E) The respiratory capacity of patient 1 fibroblasts treated with LY or RP for 12 weeks was measured using the Seahorse XFe96 extracellular flux analyser and showed a major increase in oxygen consumption under all conditions for the drug-treated cells (n = 15 of culture wells).

(F) The $NADH/NAD^+$ ratio of patient 1 fibroblasts treated with LY or RP for 12 weeks was measured under basal condition and pyruvate (i, 200 μM, 30 min) and quantified (ii; n > 180 cells). The result showed a significant decrease compared to pre-treatment levels. Scale bar = 100 μm.

(G) Acidification of the growth medium revealed by the absorption ratio of phenol red was significantly reduced after chronic drug treatments with RP and LY (i and ii; n = 9 culture wells). Lactate production normalised to glucose consumption (iii, n = 4 culture wells) was also significantly reduced. In each case, media were collected after 2 days culture of patient 1 fibroblasts treated with LY or RP for 12 weeks.

(H) Fibroblasts of patient 1 treated with LY or RP for 12 weeks were also cultured in media with a variety of glucose/galactose concentrations to further assess the glucose dependence, displayed a significant improvement of cell growth in all conditions from the drug-treated cells (n = 4-8 culture wells).

(I) BNGE were used to assess the expression of respiratory chain proteins and supercomplex assembly of patient 1 fibroblasts treated with LY or RP, showing a major increase in the assembly of almost all supercomplexes from the drug-treated cells (n = 3 independent experiments).

(J) Rates of ROS production of patient 1 fibroblasts treated with LY or RP for 12 weeks were significantly reduced to the level that no longer significantly different from controls, which was shown in Fig. 1G (n = 3 independent experiments).

All data represented as mean ± s.d. and were analysed by one/two-way ANOVA with Tukey's multiple comparisons test (* $p < 0.05$, ** $p < 0.01$, *** $p < 0.001$, **** $p < 0.0001$).

Figure S5. Inhibition of PI3K, Akt, and mTORC1 also reduced mutant load and rescued mitochondrial function in A549 cybrid cells.

(A-B) Immunoblotting (i) of the phosphoproteins (p-Akt/Akt, p-S6/S6 and p-AMPK/AMPK; A) and ISR/UPR^{mt} proteins (B) in A549 cybrid cells treated with RP (ii) or LY (iii) over 6 weeks demonstrate the effective inhibition of Akt or mTORC1 and a decrease of the ISR in the drug-treated cells (n = 3 independent experiments).

(C) The mitochondrial membrane potential of A549 cybrid cells significantly increased after exposure to LY or RP for 6 weeks (i and ii). Mitochondrial fragmentation counts (MFC, iii) were also reduced following treatment with either compound (n = 5 independent biological samples). Scale bar = 25 μm.

(D) Cell respiratory capacity of A549 cybrid cells treated with LY or RP for 6 weeks was measured using the Seahorse XFe96 extracellular flux analyser, and showed a major increase in oxygen consumption under all conditions after treatment (n = 18 culture wells).

(E-I) MK2206, an inhibitor of pan-Akt (E), treatment (1 μM) also reduced mutant load in A549 cybrid cells over 6 weeks of treatment (F, n = 3 independent experiments). Immunoblotting of p-Akt/Akt and p-S6/S6 (G) confirmed the effect of MK2206 (n = 3 independent samples). Mitochondrial membrane potential (H) and cell respiratory capacity (I, n = 8 culture wells) of A549 cybrid cells also increased after treatment with MK2206.

(J) PCR-RFLP was applied to measure the change in mutant load in 143B cybrid cells carrying the m.8993T>G mutation (N80, with 80% mutant mtDNA; N50, with 50% mutant mtDNA) treated with LY or RP for 8 weeks, showing no significant effect on the mutant load of the m.8993T>G (n = 3 independent biological samples).

(K) Cytosolic NADH:NAD$^+$ ratio of A549 cybrid cells transfected with the genetically encoded probe SoNar and treated with LY or RP for 6 weeks was measured (i) and quantified (ii) under basal condition and following exposure to pyruvate (200 μm, 30 min; n > 30 cells).

(L) The absorption ratio of phenol red was used to measure the pH of the growth media (i and ii, n=10 culture wells) and the kit of the CuBiAn instrument was used to measure lactate production (iii, n = 4 culture wells). Both acidification of the medium and lactate secretion were reduced after 2 days culture of A549 cybrid cells treated with LY or RP for 6 weeks.

(M) BNGE were used to measure supercomplex assembly and In Gel activity of A549 cybrid cells after 6 weeks of treatment with LY or RP (n = 3 independent experiments).

(N) Rates of ROS production of A549 cybrid cells treated with LY or RP for 6 weeks were reduced to the level that no longer significantly different from WT cells, which was shown in Fig. S1C-D (n = 9 culture wells).

All data represented as mean ± s.d. and were analysed by one/two-way ANOVA with Tukey's multiple comparisons test (* $p < 0.05$, ** $p < 0.01$, *** $p < 0.001$, **** $p < 0.0001$).

Figure 5. Reduction of the m.3243A>G mutant load by inhibition of PI3K-Akt-mTORC1 requires neither selective cell death nor clonal expansion and is a cell-autonomous event.

(A) A flow chart describing the cell culture process (i) used to assess cell growth/death (ii) over the 4- or 8-weeks drug treatments and single-cell PCR for the m.3243A>G mutant loads using TaqMan SNP genotyping (iii).

(B) Cell growth (i and ii) and cell death (iii and iv) over the 4- or 8-weeks drug treatments of A549 cybrid cells (i and iii) and patient 1 fibroblasts (ii and iv) were measured using the Incucyte (n=6 culture wells). Although treatment with either LY or RP at 5 µM slowed cell proliferation in both patient 1 fibroblasts and cybrid cells (i and ii), the cell death numbers were also lowered by the drug treatments (iii and iv).

(C-D) A scatter plot showing the distribution of WT and mutant mtDNA measured in single A549 cybrid cells treated with LY or RP for 4 weeks showed a clear shift of mutant load distribution. (C). Mutant load distributions of single A549 cybrid cells (i, n > 800 cells) and patient 1 fibroblasts (ii n > 500 cells) treated with LY or RP for 4 and 8 weeks, respectively.

All data represented as mean ± s.d. and were analysed by one/two-way ANOVA with Tukey's multiple comparisons test (* $p < 0.05$, ** $p < 0.01$, *** $p < 0.001$, **** $p < 0.0001$).

Figure S6. TaqMan SNP genotyping can be used at single-cell resolution to measure the distribution of mutant mtDNA burden in a cell population.

(A) Cell growth and cell death of A549 cybrid cells were measured before and after treatment with MK for 4 weeks (n = 8 culture wells). The drug had no specific effect on the mutant cells.

(B-C) TaqMan SNP genotyping was validated by measuring the mutation load in a whole population of cells (B, n = 3 independent biological samples) and then to establish the range of mutant load at the level of single cells in the A549 cybrid cells (C).

(D) Immunofluorescence staining for COXIV (i and quantified in ii) showed that the expression of COXIV in patient 1 fibroblasts was significantly lower than that of control 1 (n = 100 cells), while LY or RP treatments restored its expression (iii, n > 60 of cells). The histograms (iv and v) display the

779 heterogeneous distribution of intensities measured at the single-cell level in control 1 and patient 1
780 fibroblasts.

781 All data are represented as mean ± s.d. and were analysed by one/two-way ANOVA with Tukey's
782 multiple comparisons test (* $p < 0.05$, ** $p < 0.01$, *** $p < 0.001$, **** $p < 0.0001$).

783

784 **Figure 6. Autophagy/mitophagy is necessary to reduce the m.3243A>G mutant load following**
785 **inhibition of the PI3K-Akt-mTORC1 pathway.**

786 (A) In fibroblasts of patient 1, immunoblotting (i) of LC3B with or without CQ (50 μm for 5 h on the
787 day of experiments) over 12 weeks drug treatments (ii and iii) showed a major increase in autophagic
788 flux in drug-treated cells (n = 3 of independent experiments).

789 (B) Confocal imaging of the autophagy reporter, mCherry-GFP-LC3 (n = 25 cells) in patient 1 fibroblasts
790 treated with LY or RP at the indicated time points (i, 6 weeks, and ii, 24 h). The ratio of green/red
791 puncta (iii), autophagosome numbers (iv) and puncta size (v) were further quantified, showing a major
792 decrease in the ratio of green/red puncta and puncta size in response to the treatments. Scale bar =
793 50 μm.

794 (C) Imaging of the mitophagy reporter (i), mitoKeima, was used to specifically quantify mitophagy in
795 patient fibroblasts treated with LY, RP or CQ (10 μM). Quantification of the mitochondrial area fraction
796 engulfed in autolysosomes in both patient 1 (ii) and 2 (iii) were quantified and showed a dramatic
797 increase in mitophagy in both patient cell lines, which was completely prevented by treatment with
798 chloroquine (n = 7-10 independent biological samples).

799 (D-E) A549 cybrid cells (D) and patient 1 fibroblasts (E) were cultured with the inhibitors RP and LY as
800 in all prior experiments but in combination with CQ (10 μM), showing that CQ completely prevented
801 the decrease of mutant load in response to inhibition of the PI3K-Akt-mTORC1 pathway (n = 3
802 independent experiments).

803 (F) A scheme describing how the m.3243A>G mutation alters cell metabolism, including mitochondrial
804 dysfunction, altered glucose metabolism, redox imbalance and oxidative stress, which leads to the
805 constitutive activation of the PI3K-Akt-mTORC1 pathway and a defect in autophagy/mitophagy.
806 Pharmacological inhibition of this pathway reduces mutant load, rescues mitochondrial function and
807 reduces glucose dependence. These findings suggest that the activation of the PI3K-Akt-mTORC1
808 pathway drives a positive feedback cycle, which maintains/increases mutant mtDNA, augments the
809 metabolic rewiring and thus worsens cell signalling perturbation. This positive feedback loop may
810 shape the phenotype of the disease and determine disease progression.

All data are represented as mean ± s.d. and were analysed by one/two-way ANOVA with Tukey's multiple comparisons test (* $p < 0.05$, ** $p < 0.01$, *** $p < 0.001$, **** $p < 0.0001$).

Figure S7. Mitochondrial biogenesis and changes in mtDNA copy number do not explain the reduction of mutant mtDNA burden, while autophagy/mitophagy is also upregulated by inhibition of the PI3K-Akt-mTORC1 pathway in A549 cybrid cells.

(A) Quantitative PCR assessing mtDNA copy numbers of patient 1 fibroblasts (i) and A549 cybrid cells (ii) over the 6- or 12-weeks of treatments (n = 3 independent experiments).

(B) In A549 cybrid cells, immunoblotting of LC3B with or without CQ (50 μm for 5 h on the day of experiments) throughout drug treatments (i) showed a major increase in autophagic flux in drug-treated cells (ii and iii, n = 3 independent experiments).

(C) Imaging of mCherry-GFP-LC3 (n > 30 cells) in A549 Cybrid cells treated with LY or RP at the indicated time points (i and ii). The ratio of green/red puncta (iii), autophagosome numbers (iv) and puncta size (v) were further quantified, showing a major decrease in the ratio of green/red puncta and puncta size. Scale bar = 20 μm.

(D) Immunofluorescence staining for LC3B and cytochrome c (i) indicating that mitophagy of A549 cybrid cells was increased by LY or RP treatments (ii, n > 40 cells).

(E) Imaging of mtKeima (i) showing that mitophagy of WT fibroblasts (ii) was much higher than patient fibroblasts (compared with Fig. 6C, ii and iii).

All data are represented as mean ± s.d. and were analysed by one/two-way ANOVA with Tukey's multiple comparisons test (* $p < 0.05$, ** $p < 0.01$, *** $p < 0.001$, **** $p < 0.0001$).

METHODS

RESOURCE AVAILABILITY

Lead Contact

Further information and requests for resources and reagents should be directed to and will be fulfilled by the Lead Contact, Michael R Duchen (m.duchen@ucl.ac.uk).

Materials Availability

This study did not generate new unique reagents.

Data and Code Availability

EXPERIMENTAL MODEL AND SUBJECT DETAILS

Cell Lines

The A549 cybrid cell line derived from the fusion of enucleated patient cells harbouring the m.3243A>G mtDNA mutation was a gift from Ian Holt (Biodondostia Research Institute, San Sebastián, Spain). The 143B cybrid cell lines with ~50% and ~80% of the m.8993T>G mtDNA mutant loads were gifts from the Minczuk lab (MRC Mitochondrial Biology Unit, Cambridge, UK). Control and patient fibroblasts bearing the m.3243A>G mtDNA mutation were obtained from the MRC Centre for Neuromuscular Disorders Biobank London. The patient fibroblasts with the m.3243A>G mutation were isolated from two female subjects (mother and daughter) at the age of 59 (patient 1) and 35 (patient 2) at the time biopsies were taken. For patient 1, the clinical symptoms included diabetes, myoclonus, sensorineural hearing loss, memory decline, myopathy, pigmentary retinopathy and bipolar affective disorder. For patient 2, the symptoms included diabetes, sensorineural deafness, cerebellar ataxia, myopathy, epilepsy, depression and cognitive impairment. These cell lines were cultured in Dulbecco's modified Eagle's medium (Gibco #10566016) supplemented with 10% fetal bovine serum (Gibco #16140071), and 1% Antibiotic-Antimycotic (Gibco #15240096) and incubated at 37 °C with 5% CO_2.

860 **Human muscle biopsies**

861 The muscle biopsies were from a female patient with the m.3243A>G mutation (at the age of 55) and
862 a matched healthy control. The study was approved by the Queen Square Research Ethics Committee,
863 London (09/H0716/76). Informed consent was obtained from all participants.

864

865 **METHOD DETAILS**

866 **Cell culture and drug treatments for PI3K, Akt, or mTORC1 inhibition**

867 A549 cybrid cells (WT and mutant) and 143B cybrid cells were passaged every 3-4 days at 80%
868 confluence and trypsinised using 0.25% trypsin-EDTA (Gibco #25200056). Similarly, control and
869 patient fibroblasts were passaged every week in the same way. Media with or without drugs were
870 changed every 2-3 days. For drug treatments, rapamycin (Cayman Chemical #13346), LY294002
871 (Cayman Chemical #70920) and MK2206 (Cayman Chemical #11593) were dissolved in DMSO (Sigma-
872 Aldrich #D2650) at 10 mM stock concentrations, while chloroquine (Cayman Chemical #14194) was
873 dissolved in PBS at 50 mM for stock. Drugs were subsequently diluted to their working concentrations
874 in media. Heteroplasmy level in the A549 cybrid cells, the 143B cybrid cells and the fibroblasts of
875 patient 1 without treatments did not change significantly throughout the study as assessed by ARMS-
876 qPCR or PCR-RFLP.

877

878 **Measurements for mtDNA mutations**

879 Levels of mtDNA mutation were detected using PCR-restriction fragment length polymorphism
880 (RFLP)[16,55] or allele refractory mutation system (ARMS)-based quantitative PCR (qPCR) analysis [17]. DNA
881 extractions from frozen cells were performed using the DNeasy Blood & Tissue Kit (Qiagen #69506).
882 Concentrations of DNA samples were quantified using NanoDrop. All primer pairs used can be found
883 in the Key Resources Table. For PCR-RFLP, samples (20 ng/µl, 2 µl) were mixed with the master mixes
884 containing 1 µl primers (10 µM each) and reagents of GoTaq G2 (Promega #M7845) and the final
885 volume was 25 µl. After 30 thermocycles, amplified PCR products (8 µl) were further digested by ApaI
886 (Promega #R6361) for the m.3243A>G and HapII (Promega #R6311) for the m.8993T>G and analysed
887 by a 2% agarose gel with ethidium bromide. Densitometric analysis was performed by Fiji [56]. For ARMS-
888 qPCR, samples were diluted to 0.4 ng/µl. ARMS primer working solutions (5 µM, 1 µl each) and SYBR
889 Green JumpStart Taq ReadyMix (Sigma-Aldrich #S4438) were added together as master mixes for
890 mutant and wild-type genes. DNA samples (3 µl) and master mixes (7 µl) were pipetted into a 96-well

PCR plate (Bio-Rad #MLL9651) and PCR amplification performed using the CFX96 Touch Real-Time PCR Detection System (Bio-Rad). Each sample has three technical replicates. Mutant heteroplasmy level (%) was calculated using $1/[1 + (1/2)^{\Delta CT}] \times 100\%$, where ΔC_T (cycle threshold) = $CT_{wild\text{-}type} - CT_{mutant}$.

Quantification of relative mtDNA copy number

The relative mtDNA copy number of cells was determined using quantitative PCR with primers for the mtDNA $tRNA^{Leu(UUR)}$ and with primers for the nuclear B2-microglobulin as previously described [57]. Standard 96 well PCR plate with optically clear sealing film and CFX96 Real-Time PCR Detection System (Bio-Rad) were used. PCR mix consists of 2 µl of template DNA (3 ng/µl), 2 µl of primer pair (final concentration of 400 nM), 12.5 µl of SYBR Green JumpStart Taq ReadyMix (Sigma-Aldrich) and 8.5 µl of DNase/RNase free H_2O. The thermal cycling conditions were as follow: 50 °C for 2 min, 95 °C for 10 min and then 40 cycles of 95 °C for 15 s and 62 °C for 1 min. Each sample has three technical replicates. The following equation was used to determine the relative mitochondrial DNA content, $2 \times 2^{\Delta CT}$, where ΔC_T is nuclear DNA CT value subtracted by mtDNA CT value.

The mitochondrial oxygen consumption rate

Measurements of aerobic respiration and glycolysis were conducted with the Seahorse Bioscience XFe-96 bioanalyzer using the Seahorse XF Cell Mito Stress Test Kit (Agilent #103015-100). Cells were seeded on XF96 cell culture microplates (Agilent #102416-100) two days before the experiment (A549 cybrid cells, 1×10^4 cells/well; Fibroblasts, 2×10^4 cells/well). On the day of the experiment, the culture medium was replaced with Seahorse XF Base medium (Agilent #103334-100) supplemented with 1 mM pyruvate (Gibco #11360070), 2 mM glutamine (Gibco #25030081) and 10 mM glucose (Gibco #A2494001) and incubated for 30 min at 37 °C in a CO_2-free incubator before loading into the Seahorse Analyzer. After measuring basal respiration, the drugs oligomycin (5 µM), FCCP (1 µM, 2 µM), and rotenone/antimycin A (0.5 µM/0.5 µM) were added to each well in sequential order. Data were analysed using the XF Cell Mito Stress Test Report Generator. After the assay, cells were stained with Hoechst 33342 (5 µM; Thermo Scientific #62249) for 30 min. ImageXpress was then used to count the numbers of cell nuclei (cell numbers) in each well. The normalisation of the experiments is based on the relative cell numbers obtained.

Mitochondrial membrane potential, $\Delta\psi_m$, and the mitochondrial fragmentation count

Cells were seeded (3 x 10^4/well for A549 cybrid cells; 1 x 10^4/well for fibroblasts) in glass-bottom 24-well plates, 2-3 days before imaging. Cells were washed twice with the recording medium, which was phenol red-free DMEM (Gibco #A1443001) with 10 mM glucose, 1 mM glutamine, 10 mM HEPES, adjusted to pH 7.4; and then incubated with 25 nM tetramethylrhodamine methyl ester (TMRM) for 30 min at 37 °C. Cells were imaged with an LSM 880 (Carl Zeiss) confocal microscope using Fluar 63x/1.40 oil immersion objective lens at 37 °C. TMRM was excited with a 561 nm Argon laser with an output power of 0.2 mW. MBS 488/561 was used as a beam splitter and emitted fluorescence collected at 564-740 nm. Images were acquired using Zen Black software (Carl Zeiss) and fluorescence intensity was quantified using Fiji with the same threshold across all samples. To quantitatively describe mitochondrial morphology, mitochondrial network fragmentation according to Rehman et al., 2012 was applied. Briefly, thresholding images were binarized and mitochondrial structure of each cell was count with the particle counting and normalised to the total mitochondrial area (μm^2) per cell to obtain the mitochondrial fragmentation count (MFC). To be specific, MFC = (number of particles x 100)/total mitochondrial area.

ROS measurements

Rate of general ROS production was assessed using dihydroethidium (DHE, Invitrogen #D11347), an intracellular superoxide indicator which is oxidised by superoxide to ethidium which fluoresces red. As for mitochondrial ROS production, MitoSOX (Invitrogen #M36008) was used. One day before the experiment, cells were seeded in a glass-bottom 96-well plate (SensoPlate #655892) at a density of 2 x 10^4 cells per well. On the day of the experiment, cells were washed twice with PBS and incubated with 5 µM DHE or MitoSOX in recording medium (phenol red-free DMEM, 10 mM glucose, 1 mM glutamine, 10 mM HEPES, adjusted to pH 7.4). Measurements of fluorescence intensity were taken at intervals of 5 min at 37 °C using the CLARIOstar microplate reader (excitation/emission = 518/606 nm for DHE excitation/emission = 510/580 nm for MitoSOX). The total incubation time for DHE is 1 h and 30 min for MitoSOX. The slope of fluorescence intensity was calculated (Fig. S1C) and represents the rate of ROS production.

Glucose uptake using 2-NBDG

A fluorescent deoxyglucose analogue, 2-NBDG (Invitrogen #N13195), was employed as a probe to measure rates of glucose uptake by cultured cells. Cells were seeded in a glass-bottom 96-well plate as ROS measurements. On the day of experiments, cells were firstly washed with glucose-free recording media twice and incubated with the glucose-free media for 1 h. After media aspiration, recording media with 2-NBDG (100 µg/ml) were then added into wells and incubated for 30 min. After the incubation, cells were then again washed with glucose-free recording media twice and fluorescence intensity were measured using the CLARIOstar microplate reader (excitation/emission = 467/542 nm).

Medium pH values

Medium pH values were measured based on the ratiometric property of phenol red, a common pH indicator in media. The absorbance of phenol red change in response to changing pH. Cells were seeded in 96-well plates at a density of 1 x 10^4 cells per well with 200 µl media and cultured for 2 days. On the day of experiments, media of each well were then transferred to a new 96-well plate and measured the absorbance of phenol red at 443 and 570 nm immediately. The higher the absorbance ratios of 443 to 570 nm, the more acidic the media.

Glucose and lactate concentrations in media using CuBiAn

Media for pH measurements were then directly used for quantifying glucose and lactate concentrations in media. Samples and fresh media were measured using the CuBiAn HT-270 biochemistry analyser (Optocell technology) with its Glucose (#200106) and Lactate Assay Kits (#200115) according to manufacturer instructions.

Blue native gel electrophoresis (BNGE) and In Gel activity assays

Mitochondria were isolated from cultured fibroblasts and cell lines according to the method described earlier (ref). Digitonin-solubilized mitochondria proteins (100 µg) were separated on pre-cast 3%-12% gradient blue native gels (Invitrogen #BN1001) according to manufacturer's instructions. After electrophoresis, the gels were electroblotted onto PVDF membrane (Millipore #IPVH00010) and probed with anti-OxPhos antibody cocktail (1:1000, Invitrogen #45-8199), anti-SDHA (1:1000, Abcam #ab137040) and anti-ATP5A (1:1000, Abcam #ab14748). The enzymatic activity of different OxPhos

complexes was determined by in-gel assays. For CIV+CI activity, the gels were incubated first in CIV substrate (50 mg diaminobenzidine and 100 mg cytochrome c in 50 mM phosphate buffer, pH 7.4) until brown signal was observed and then incubated in CI substrate (0.1 mg/ml NADH, 2.5 mg/ml Nitrotetrazolium Blue chloride in 100 mM Tris–HCl, pH 7.4) until blue signal appeared. The reaction was stopped with 10% acetic acid and the gels were washed and scanned.

SDS-PAGE and immunoblotting

For immunoblotting, cells were seeded 1-day prior experiments (60 mm plates for the A549 cybrid cells and 10 cm plates for fibroblasts). To assess autophagic flux, cells were replenished with regular media for 1 h to prevent starvation-induced autophagy. After 1 h, treatment conditions resumed either with or without 50 µM chloroquine for 6 h. For other experiments, cells were then washed with ice-cold PBS once and lysed using 150-300 µl RIPA buffer (Sigma-Aldrich #R0278) with one cOmplete™ Protease Inhibitor Cocktail (Roche #4693116001) tablet and one PhosSTOP Phosphatase Inhibitor Cocktail (Roche #4906837001) tablet. Cells were then scraped and centrifuged at 16,000 g at 4 °C for 30 min. Protein concentration in the supernatant was quantified using the Pierce BCA Assay Kit (Thermo Scientific #23227). For immunoblotting, 30 µg of protein samples in NuPAGE 4x LDS Sample Buffer (Invitrogen #NP0007) and 2% β-mercaptoethanol (Sigma-Aldrich #63689) were boiled at 99ºC for 5 min. Proteins were separated on 4-12% NuPAGE Bis-Tris polyacrylamide gels (Invitrogen #NP0335) immersed in MOPS running buffer (Invitrogen #NP0001) and transferred onto PVDF membranes (Millipore #IPFL00010). Membranes were then incubated in Intercept (TBS) Blocking Buffer (Li-COR Biosciences #927-60001) for 1 h at room temperature. After addition of primary antibodies diluted in the blocking buffer with 0.1% Tween-20, membranes were incubated overnight at 4ºC on a shaker. Subsequently, membranes were incubated with appropriate secondary antibodies (Li-COR Biosciences; 1:10000; IRDye® 680RD Goat anti-Mouse IgG, #926-68070; IRDye® 800CW Goat anti-Rabbit IgG, #926-32211) for 1 h at room temperature before signals were developed with the LiCOR Odyssey CLx system. Densitometry analysis was performed using Fiji. Details of all the antibodies used in this study can be found in the Key Resources Table. Following is the antibodies and dilutions for immunoblotting: Anti-PC (1:1000, Novus Biologicals #NBP1-49536), anti-phospho-PDHA (1:1000, Millipore #AP1062), anti-PDHA (1:1000, Invitrogen #45-6600), anti-p-Akt (1:1000, Cell Signaling Technology #9271), anti-Akt (1:3000, Cell Signaling Technology #9272), anti-p-S6 (1:3000, Cell Signaling Technology #4858), anti-S6 (1:3000, Cell Signaling Technology #2217), anti-p-AMPK (1:1000, Cell Signaling Technology #2532), anti-AMPK (1:3000, Cell Signaling Technology #2532), anti-LC3B (1:3000, Cell Signaling Technology #3868), anti-p-eIF2α (1:1000, Cell Signaling Technology

#9721), anti-eIF2α (1:3000, Cell Signaling Technology #9722), anti-ATF4 (1:1000, Cell Signaling Technology #11815), anti-ATF5 (1:1000, Abcam #ab60126), anti-CHOP (1:1000, Santa Cruz Biotechnology #sc-7351), and anti-β-actin (1:10000, Santa Cruz Biotechnology #sc-47778).

Live-cell imaging for cell growth and death using the Incucyte platform

Cells were seeded at a density of 2,000 cells/well in a 96-well plate one-day prior imaging with regular cell culture media. For cell growth/death in a variety of nutrient conditions, cells were washed with PBS twice and then DMEM (Gibco #11966025 or #11960044) with different concentration of glucose, galactose (Sigma-Aldrich #G5388) or glutamine and 10% dialysed FBS (Sigma-Aldrich #F0392) were added. For drug treatments, media were then replaced with fresh media with/without drugs along with 20 nM SYTOGreen Nucleic Acid Stain (Invitrogen #S7572) just before imaging. Images were acquired using the Incucyte with 20X objective every 2 h for a 3-4 days period. Cell confluency and cell death numbers were analysis on Incucyte software and sequentially extracted. Rates of cell growth were analysed by fitting the growth curve to the exponential cell growth model (Fig. S1E) using the solver in Excel, while cell death was obtained by simply normalising the numbers of dead cells (SYTOGreen stained) to total cell confluency.

Measurements of cytosolic NADH:NAD$^+$ using SoNar

The genetically encoded probes, SoNar for NADH:NAD$^+$ ratio, were developed by and obtained from the Yang's Lab (Chinese Academy of Sciences) [18]. For A549 cybrid cells, the cells were seeded at the density of 4 x 10^4/well in glass-bottom 24-well plates two days before transfection. Lipofectamine 3000 (Invitrogen #L3000001) was used for transfection according to the manufacturer's protocol. Specifically, we used 1 µg DNA and the ratio of p3000 to the 3000 reagent was 2:1. The cells were imaged two days after transfection in recording media with the LSM 880 microscope using 20x/0.8 objective lens at 37ºC. Both probes were excited at 405 and 488 separately and emitted fluorescence longer than 535 nm was collected. For fibroblasts, Human Dermal Fibroblasts Nucleofector Kit (Lonza #VPD-1001) was used for transfection according to the manufacturer's protocol. Specifically, we used 2.5 µg DNA for 5 x 10^5 cells. Similarly, fibroblasts were imaged two days after transfection with the same conditions as A549 cybrid cells. Images were acquired using Zen Black software (Carl Zeiss) and analysed using Fiji. Regions of interest (ROI) were generated by thresholding and binarizing images and average fluorescence intensity in the ROIs for each channel were then measured. Ratios between the signal excited at 405 nm and 488 nm were calculated.

Measurement of autophagy and mitophagy using mCherry-EGFP-LC3 and mt-Keima, respectively

The autophagy reporter, mCherry-EGFP-LC3 (Addgene plasmid #22418), and mitophagy reporter, mt-Keima (Addgene plasmid #56018) were purchased from Addgene. The procedure of transfection for A549 cybrid cells and patient fibroblasts was similar to SoNar. Imaging was performed with the LSM 880 microscope using 63x/1.40 oil immersion objective lens at 37 °C. The mCherry-EGFP-LC3 was excited at 488 and 561 nm separately and emitted fluorescence 500-580 and longer than 600 nm was collected. Images were acquired using Zen Black software (Carl Zeiss). Numbers and area of fluorescent particles for each channel were quantified using Fiji by thresholding images. For mt-Keima, following transfection, the cells were treated as indicated for 24h and imaged via two sequential excitations (458 nm, green; 561 nm, red) using a 570- to 695-nm emission range. The laser power was set at the minimum output to allow the clear visualization of the mt-Keima signal and was separately adjusted for each experimental conditions. At least 10 z-stacks with 0.45 um thickness were acquired per sample in an experimental set. LysoTracker Green DND-26 (Invitrogen #L7526) was co-imaged using a 488 nm excitation and a 495-550 nm emission filter, where indicated. The ratio (high F_{543}/F_{458} ratio area/total mitochondrial area) was used as an index of mitophagy. Ratio (F_{543}/F_{458}) images were generated using the Ratio Plus plugin in Fiji. High (F_{543}/F_{458}) ratio areas and total mitochondrial area were binarized, segmented and quantified in Fiji.

Metabolomics

Control and patient fibroblasts were plated 24 hrs before the experiment in 10 cm dishes (1 x 10^6 cells/dish). On the day of experiments, the medium was replaced with phenol red-free DMEM with 1 mM glutamine, 10% dialysed FBS (prepared as described in Yuneva et al., 2007) and 10 mM [U-^{13}C]-glucose (Goss Scientific #CLM-1396-1). After 24 h incubation, cells were washed once with ice-cold PBS. Metabolites were extracted with adding 500 µl of ice-cold methanol, scraping, and transferring into tubes on ice. Dishes were then subsequently washed with 250 µl methanol and 250 µl water containing 2.5 nM of each nor-leucine and scyllo-inositol per sample as internal standards. Finally, 250 µl of chloroform was added and samples were sonicated for 3 rounds (8 min each) at 4 °C. After centrifugation (18,000 g for 10 min at 4 °C), the upper polar fraction was collected and used for GC-MS analysis, while he protein pellets were dried, lysed using 62.5 mM Tris buffer (pH 6.8) containing 2% SDS and used for protein quantification using BCA assay (Abcam). Briefly, the polar fraction was washed twice with methanol, derivatized by methoximation (Sigma, 20 µl, 20 mg/ml in pyridine) and

trimethylsilylation (20 µl of N,O-bis(trimethylsilyl) trifluoroacetamide reagent (BSTFA) containing 1% trimethylchlorosilane (TMCS), Supelco), and analysed on an Agilent 7890A-5975C GC–MS system. Splitless injection (injection temperature 270 °C) onto a 30 m + 10 m × 0.25 mm DB-5MS + DG column (Agilent J&W) was used, using helium as the carrier gas, in electron ionization (EI) mode. The initial oven temperature was 70 °C (2 min), followed by temperature gradients to 295 °C at 12.5 °C/min and then to 320 °C at 25 °C/min (held for 3 min). Data analysis and peak quantifications were performed using MassHunter Quantitative Analysis software (B.06.00 SP01, Agilent Technologies). The level of labelling of individual metabolites was corrected for the natural abundance of isotopes in both the metabolite and the derivatization reagent. Abundance was calculated by comparison to responses of known amounts of authentic standards [60]. The data were further processed and visualised by MetaboAnalyst 4.0, using the Pathway Analysis module with the library of human SMPDB and the Metabolite Set Enrichment Analysis with the library of predicted metabolite sets [61].

Lipidomics

Fibroblasts for lipid extraction were grown in 15 cm dishes in DMEM medium supplemented with 1% FBS until fully confluent. When confluent, cells were counted and about 10^6 cells were washed and lysed in 0.5 ml water on ice for 5 min. A Folch extraction was performed: 3ml of chloroform/methanol (2/1) was added to separate lipids in the organic phase and the solution was centrifuged at 4 °C for 30 min. The organic phase was collected and stored in glass vials at -80 °C until the mass spectrometry analysis was performed. Before MS analysis, chloroform and methanol were evaporated and dried lipids resuspended in 150 µl MeOH/$CHCl_3$ 8:2. LC-MS measures were carried out by HPLC (Model 1100 series; Hewlett-Packard) coupled to a quadrupole ion-trap mass spectrometer (Esquire-LCTM; Bruker, Bremen, Germany) equipped with an electrospray ion source (ESI), in both positive and negative ion-modes. Chromatographic separation of the lipids was carried out at 303 K on a C18 column by injecting 5 µl of the 4 lipid raw extracts (3 biological replicates for each sample) into the column (Kinetex TMC18; length, 100 mm; particle size, 2.6 µm; internal diameter, 2.1 mm; pore size, 100 Å; Phenomenex, Torrence, CA, USA). The solvent system consisted of eluent A as CH_3OH/H_2O (7:3, v/v) containing 12 mM ammonium acetate, and eluant B as CH_3OH also containing 12 mM ammonium acetate. The linear gradient was run at a constant flow rate of 0.3 ml/min, and went from 30% B to 100% B in 40 min. This was followed by the column wash using 100% B for 15 min, and then column re-equilibration under the starting conditions (i.e., 30% B). The nebuliser gas was high purity nitrogen at a pressure of 20 psi to 30 psi, at a flow rate of 6 L/min and 300 °C. The MS scan range was 13,000 U/s in the range of 50 m/z to 1500 m/z, with a mass accuracy of ≈ 100 ppm. The ESI was operated in

positive ion mode for the qualitative and quantitative analysis of lyso-GPC, GPC and SM, and both in positive and negative ion mode for glycerol-phospholipids classes GPI and GPE. For the structural assignment of the lipid species, the extracted ion chromatograms from the positive and/or negative ion full scan data were integrated using the DataAnalysis 3.0 software (Bruker Daltonik, Bremen, Germany). In particular, for PE, negative ion mode provided a good yield of molecular ions and information on the length and unsaturation index of the fatty acyl chains, while positive ion mode was used to confirm the correct assignment by analysis of the neutral loss of the polar head. The lipid quantitation was performed by integration of the extracted ion chromatograms (XIC), achieved through the proprietary software Bruker Daltonics esquireLC 4.5. Overall, the following lipid classes were detected: lysophosphatidylcholines (Lyso-GPC), glycerophosphatidylcholines (GPC), plasmenyl phosphatidylcholines (plasmenyl-GPC), sphingomyelins (SM), glycerophosphatidylethanolamines (GPE), plasmenly phosphatidylethanolamines (plasmenyl-GPE), glycerophosphatidylinositols (GPI), ceramides, and triacylglycerols (TAG), cholesteryl-esters and cholesterol. To compare across samples the results within a given lipid class, data were normalized with respect the total ion current (TIC) of this class (relative intra-class quantitation) whilst to compare the results among different lipid classes the corresponding signal areas were normalized to the total area of different classes in different runs (normalization to the relative protein amount leads to similar conclusions). Normalized MS data were further processed and visualised by MetaboAnalyst 4.0, using the Pathway Analysis module with the library of human SMPDB.

Nile Red O imaging

Fibroblasts were plated on imaging coverslips and grown in DMEM medium supplemented with 1% FBS. After 24 hours, cells were incubated for 5 min with 0.1 µg/ml of Nile Red O (Sigma-Aldrich #72485) dissolved in imaging buffer [62]. Live cell imaging was performed on a Zeiss 880 confocal microscope, equipped with a 40x objective and exciting cells at 488 nm and collecting fluorescence longer than 530 nm. Image analysis was performed using Fiji to evaluate the number of Nile Red positive puncta, likely lipid droplets, and their areas for each cell that was imaged.

RNA-sequencing

Fibroblasts for RNA-sequencing were plated in 10 cm dishes with regular media (1 x 10^6 cells/dish) one day before RNA extraction. RNA extractions were performed using the RNeasy Mini Kit (Qiagen #74104). Concentrations and quality of RNA samples were quantified using NanoDrop (total RNA >250

ng, A_{260}/A_{280} = 1.8-2.1, A_{260}/A_{230} > 1.7). RNA-sequencing was then performed at UCL Genomics and analysed by the SARTools R package [63]. The resulting datasets were further analysed by Ingenuity Pathway Analysis (IPA, Qiagen) with a threshold of FDR < 0.05 and visualised by Morpheus (https://software.broadinstitute.org/morpheus) for heatmaps and NetworkAnalyst 3.0 [64] for volcano plots and principal component analysis.

Immunohistochemistry

For immunohistochemistry, muscle biopsies were fixed in phosphate buffered saline (PBS) and fixed in 4% paraformaldehyde (PFA), made in PBS, for 4-8 h at room temperature (RT). Following fixation, tissues were cryoprotected in 30% sucrose in Diethyl Pyrocarbonate (DEPC) treated PBS, embedded and frozen in a mixture of 15% sucrose /50% Tissue-Tek OCT (Sakura Finetek), and sectioned in the coronal plane at 20 µm using a Cryostat (Bright Instruments). Patient muscle biopsies sections were washed in PBS, blocked in a solution of 5% normal goat serum (Merck KGaA) (v/v) containing 0.1% Triton X-100 (v/v) (Merck KGaA) in PBS at RT for 2 h. They were first incubated in primary antibodies at RT overnight. The following antibodies were used: pan-AKT (1:200, Cell Signaling Technology #2920), phospho-AKT (p-AKT; 1:200, Abcam #ab81283), S6 (1:200), and phospho-S6 (1:200). Following incubation in primary antibodies, sections were washed in PBS, incubated in biotinylated anti-species secondary antibodies (1:250; Vector Laboratories) for 2 h. Sections were washed and incubated with bisbenzimide (10 min in 2.5 µg/ml solution in PBS; Merck KGaA). Images were collected using an SP2 Leica confocal microscope (Leica Microsystems, UK). Sequential images were subsequently reconstructed using Metamorph imaging software (Universal Imaging Corporation, West Chester, PA).

Immunofluorescence

For A549 cybrid cells, the cells were seeded at 1 x 10^5 cells per well in 6-well plates on 22 mm glass coverslips. On the day of the experiment, cells were replenished with regular media for 1 h to prevent starvation-induced autophagy. After 1 h, treatment conditions resumed either with or without 50 µM chloroquine for 6 h. The cells were then washed with PBS twice and fixed in 4% paraformaldehyde for 20 mins at room temperature and permeabilised with 0.2% Triton X-100 in PBS for 5 min. Following washes with 0.2% Triton X-100 PBS, coverslips were incubated with primary anti-LC3B for autophagosomes/lysosomes (1:500) and anti-cytochrome c for mitochondria (1:200, BD Pharmingen #556432) antibodies in 3% BSA 0.2% Triton X-100 PBS at 4 °C overnight. The following day, cells were washed with 0.2% Triton X-100 PBS and incubated with Alexa Fluor 488-conjugated (goat anti-rabbit,

1:200) and Alexa Fluor 647-conjugated (donkey anti-mouse, 1:500) secondary antibodies for visualisation of the lysosomes and mitochondria, respectively for 1 h. Following three PBS washes, the nucleus was counterstained using 5 µg/mL Hoechst 33342 solution diluted 1:2000 in 0.2% Triton X-100 PBS for 5 min. The coverslips were washed one final time with 0.2% Triton X-100 PBS and mounted on a glass slide using Fluoromount-G mounting medium (SouthernBiotech), stored at 4 °C until imaging. Imaging was performed with the LSM 880 microscope using 63x/1.40 oil immersion objective lens. For tricolour imaging, Hoescht 33342 was excited at 405 nm, Alexa Fluor 488 at 488 nm and Alexa Fluor 647 at 633 nm. Emitted fluorescence was collected at 410-480 nm, 500-650 nm and longer than 660 nm. Images were acquired using Zen Black software (Carl Zeiss). Image acquisition parameters settings were maintained for all samples within the experimental set. The colocalisation coefficient (Pearson's R value) of 647 nm and 488 nm emission signals, LC3B and cytochrome c, was quantified using Coloc 2 in Fiji.

For fibroblasts, cells were seeded at a density of 5 x 10^4 cells/well in 24 well plates on 10 mm coverslips. After 24h incubation, cells were treated with LY or RP for 4 weeks and 8 weeks respectively. After the long-term treatment, the cells were washed thrice with 1X PBS and fixed in 4% paraformaldehyde for 15 mins at room temperature and permeabilised with 0.1% Triton-X 100 for 15 min in PBS. The cells were then washed and incubated with anti-MTCOI antibody (1:100, Abcam #ab14705) in 3% BSA for 1h at the room temperature followed by incubation with Alexa Fluor 488-conjugated secondary antibody for 1h at the room temperature. After antibody labelling, the coverslips were mounted on a glass slide using ProLong™ Gold Antifade mountant with DAPI and imaged using the confocal microscope as described above.

TaqMan SNP genotyping for Single cell qPCR

Primers for distinguishing WT and the m.3243A>G mutant mtDNA were designed by submitting the region of the m.3243A>G mutation (~120 bp) to the website of online Custom TaqMan® Assay design tool (https://www.thermofisher.com/order/custom-genomic-products/tools/genotyping/) The Custom TaqMan SNP Genotyping Kit (Applied Biosystems #4332073) was ordered and prepared according to manufacturer instructions. For single cell sorting, cells were resuspended (1 x 10^6 cells/ml for A549 cybrid cells; 5 x 10^5 cells/ml for fibroblasts) in 1 ml PBS with 1% FBS, filtered through 70 µm mesh and then kept on ice. Sorting cells to 96-well PCR plates using BD FACS Aria Fusion was performed by Flow Cytometry Core Facility, Division of Medicine at UCL. Cells in 96-well plates were lysed with 2 µl of 0.2% Triton X-100 and kept in -80 °C immediately. For qPCR, TaqPath ProAmp Master

Mix (Applied Biosystems #A30866) was mixed with primers of TaqMan SNP genotyping and added into 96-well PCR plates to reach a final volume of 10 µl in each well. Thermo cycles were set according to manufacturer instructions. Mutant loads were determined by the ratio of mutant to total fluorescent intensity.

QUANTIFICATION AND STATISTICAL ANALYSIS

All statistical analyses, unless otherwise stated in figure legends, were carried out using GraphPad Prism 8. To compare means between two groups, a two-tailed unpaired t-test was used for normally distributed data. One/two-way ANOVA with Tukey's multiple comparisons test was performed for multi-group (at least three) comparisons. Data are presented as graphs displaying mean ± s.d., of at least three independent biological replicates. Means of control samples on immunoblotting or immunofluorescence are typically centred at one (or 100%) to ensure easier comparisons unless otherwise noted. Differences were only considered to be statistically significant when the *p* value was less than 0.05. Estimated p values are either stated as the actual values or denoted by * $p < 0.05$, ** $p < 0.01$, *** $p < 0.001$, **** $p < 0.0001$.

For detailed processing and statistical analysis of RNA sequencing, metabolomics and lipidomics, please find them in the previous section with the same subheadings.

No statistical method was used to predetermine sample size, and replicates are shown in Figure legends. The investigators were not blinded to allocation during experiments and outcome assessment.

1228 **REFERENCES**

1229 1. Gorman, G. S. *et al.* Prevalence of nuclear and mitochondrial DNA mutations related to adult
1230 mitochondrial disease. *Ann. Neurol.* (2015) doi:10.1002/ana.24362.

1231 2. Russell, O. M., Gorman, G. S., Lightowlers, R. N. & Turnbull, D. M. Mitochondrial Diseases:
1232 Hope for the Future. *Cell* **181**, 168–188 (2020).

1233 3. Craven, L., Alston, C. L., Taylor, R. W. & Turnbull, D. M. Recent Advances in Mitochondrial
1234 Disease. *Annu Rev Genomics Hum Genet* **18**, 257–275 (2017).

1235 4. Schon, E. A., DiMauro, S. & Hirano, M. Human mitochondrial DNA: roles of inherited and
1236 somatic mutations. *Nat Rev Genet* **13**, 878–890 (2012).

1237 5. Szczepanowska, J., Malinska, D., Wieckowski, M. R. & Duszynski, J. Effect of mtDNA point
1238 mutations on cellular bioenergetics. *Biochim. Biophys. Acta - Bioenerg.* **1817**, 1740–1746
1239 (2012).

1240 6. Stewart, J. B. & Chinnery, P. F. The dynamics of mitochondrial DNA heteroplasmy:
1241 implications for human health and disease. *Nat. Rev. Genet.* **16**, 530 (2015).

1242 7. Maeda, K. *et al.* Clinical Phenotype and Segregation of Mitochondrial 3243A>G Mutation
1243 in 2 Pairs of Monozygotic Twins. *JAMA Neurol.* **73**, 990–993 (2016).

1244 8. Picard, M. & Hirano, M. Disentangling (Epi)Genetic and Environmental Contributions to the
1245 Mitochondrial 3243A>G Mutation Phenotype: Phenotypic Destiny in Mitochondrial
1246 Disease? *JAMA Neurol.* **73**, 923–925 (2016).

1247 9. Valera-Alberni, M. & Canto, C. Mitochondrial stress management: a dynamic journey. *Cell*
1248 *Stress* **2**, 253–274 (2018).

1249 10. Kotiadis, V. N., Duchen, M. R. & Osellame, L. D. Mitochondrial quality control and
1250 communications with the nucleus are important in maintaining mitochondrial function and
1251 cell health()(). *Biochim. Biophys. Acta* **1840**, 1254–1265 (2014).

1252 11. Gilkerson, R. W. *et al.* Mitochondrial autophagy in cells with mtDNA mutations results from
1253 synergistic loss of transmembrane potential and mTORC1 inhibition. *Hum Mol Genet* **21**, 978–
1254 990 (2012).

1255 12. Morán, M. *et al.* Bulk autophagy, but not mitophagy, is increased in cellular model of

mitochondrial disease. *Biochim. Biophys. Acta - Mol. Basis Dis.* **1842**, 1059–1070 (2014).

13. Deus, C. M., Yambire, K. F., Oliveira, P. J. & Raimundo, N. Mitochondria–Lysosome Crosstalk: From Physiology to Neurodegeneration. *Trends Mol. Med.* **26**, 71–88 (2020).

14. Plotegher, N. & Duchen, M. R. Mitochondrial Dysfunction and Neurodegeneration in Lysosomal Storage Disorders. *Trends Mol. Med.* **23**, 116–134 (2017).

15. Cotán, D. *et al.* Secondary coenzyme Q10 deficiency triggers mitochondria degradation by mitophagy in MELAS fibroblasts. *FASEB J.* **25**, 2669–2687 (2011).

16. Nigou, M., Parfait, B., Clauser, E. & Olivier, J. L. Detection and quantification of the A3243G mutation of mitochondrial DNA by ligation detection reaction. *Mol. Cell. Probes* **12**, 273–282 (1998).

17. Wang, J., Venegas, V., Li, F. & Wong, L. J. Analysis of mitochondrial DNA point mutation heteroplasmy by ARMS quantitative PCR. *Curr Protoc Hum Genet* **Chapter 19**, Unit 19 6 (2011).

18. Zhao, Y. *et al.* SoNar, a Highly Responsive NAD+/NADH Sensor, Allows High-Throughput Metabolic Screening of Anti-tumor Agents. *Cell Metab* **21**, 777–789 (2015).

19. El-Hattab, A. W., Adesina, A. M., Jones, J. & Scaglia, F. MELAS syndrome: Clinical manifestations, pathogenesis, and treatment options. *Mol. Genet. Metab.* **116**, 4–12 (2015).

20. Golla, S., Ren, J., Malloy, C. R. & Pascual, J. M. Intramyocellular lipid excess in the mitochondrial disorder MELAS. *Neurol. Genet.* **3**, e160 (2017).

21. Manning, B. D. & Toker, A. AKT/PKB Signaling: Navigating the Network. *Cell* **169**, 381–405 (2017).

22. N'Diaye, E.-N. *et al.* PLIC proteins or ubiquilins regulate autophagy-dependent cell survival during nutrient starvation. *EMBO Rep.* **10**, 173–179 (2009).

23. Suomalainen, A. & Battersby, B. J. Mitochondrial diseases: the contribution of organelle stress responses to pathology. *Nat Rev Mol Cell Biol* **19**, 77–92 (2018).

24. Shpilka, T. & Haynes, C. M. The mitochondrial UPR: mechanisms, physiological functions and implications in ageing. *Nat. Rev. Mol. Cell Biol.* **19**, 109–120 (2018).

25. Quirós, P. M. *et al.* Multi-omics analysis identifies ATF4 as a key regulator of the

mitochondrial stress response in mammals. *J. Cell Biol.* **216**, 2027–2045 (2017).

26. Deng, J. *et al.* RNA-seq profiling, and impaired autophagic process in skeletal muscle of MELAS. *Biochem. Biophys. Res. Commun.* **523**, 91–97 (2020).

27. Gaude, E. *et al.* NADH Shuttling Couples Cytosolic Reductive Carboxylation of Glutamine with Glycolysis in Cells with Mitochondrial Dysfunction. *Mol. Cell* **69**, 581-593.e7 (2018).

28. Molenaars, M., Daniels, E. G., Meurs, A., Janssens, G. E. & Houtkooper, R. H. Mitochondrial cross-compartmental signalling to maintain proteostasis and longevity. *Philos. Trans. R. Soc. B Biol. Sci.* **375**, 20190414 (2020).

29. Mick, E. *et al.* Distinct mitochondrial defects trigger the integrated stress response depending on the metabolic state of the cell. *Elife* **9**, (2020).

30. Garrido-Maraver, J. *et al.* Critical role of AMP-activated protein kinase in the balance between mitophagy and mitochondrial biogenesis in MELAS disease. *Biochim Biophys Acta* **1852**, 2535–2553 (2015).

31. Koromilas, A. E. & Mounir, Z. Control of oncogenesis by eIF2α phosphorylation: implications in PTEN and PI3K–Akt signaling and tumor treatment. *Futur. Oncol.* **9**, 1005–1015 (2013).

32. Janssen, G. M. C. *et al.* The A3243G tRNALeu(UUR) mutation induces mitochondrial dysfunction and variable disease expression without dominant negative acting translational defects in complex IV subunits at UUR codons†. *Hum. Mol. Genet.* **16**, 2472–2481 (2007).

33. Suen, D.-F., Narendra, D. P., Tanaka, A., Manfredi, G. & Youle, R. J. Parkin overexpression selects against a deleterious mtDNA mutation in heteroplasmic cybrid cells. *Proc. Natl. Acad. Sci.* **107**, 11835 LP – 11840 (2010).

34. Kandul, N. P., Zhang, T., Hay, B. A. & Guo, M. Selective removal of deletion-bearing mitochondrial DNA in heteroplasmic Drosophila. *Nat. Commun.* **7**, 13100 (2016).

35. Wojewoda, M., Duszyński, J. & Szczepanowska, J. NARP mutation and mtDNA depletion trigger mitochondrial biogenesis which can be modulated by selenite supplementation. *Int. J. Biochem. Cell Biol.* **43**, 1178–1186 (2011).

36. de Andrade, P. B. M. *et al.* Diabetes-associated mitochondrial DNA mutation A3243G impairs cellular metabolic pathways necessary for beta cell function. *Diabetologia* **49**, 1816–1826 (2006).

37. Chen, Q. *et al.* Rewiring of Glutamine Metabolism Is a Bioenergetic Adaptation of Human Cells with Mitochondrial DNA Mutations. *Cell Metab.* **27**, 1007-1025.e5 (2018).

38. Cappel, D. A. *et al.* Pyruvate-Carboxylase-Mediated Anaplerosis Promotes Antioxidant Capacity by Sustaining TCA Cycle and Redox Metabolism in Liver. *Cell Metab.* **29**, 1291-1305.e8 (2019).

39. Raimundo, N. *et al.* Mitochondrial Stress Engages E2F1 Apoptotic Signaling to Cause Deafness. *Cell* **148**, 716–726 (2012).

40. Hoxhaj, G. & Manning, B. D. The PI3K–AKT network at the interface of oncogenic signalling and cancer metabolism. *Nat. Rev. Cancer* **20**, 74–88 (2020).

41. Castellano, B. M. *et al.* Lysosomal cholesterol activates mTORC1 via an SLC38A9–Niemann-Pick C1 signaling complex. *Science (80-.).* **355**, 1306 LP – 1311 (2017).

42. Yambire, K. F. *et al.* Mitochondrial biogenesis is transcriptionally repressed in lysosomal lipid storage diseases. *Elife* **8**, e39598 (2019).

43. Lin, Y.-F. *et al.* Maintenance and propagation of a deleterious mitochondrial genome by the mitochondrial unfolded protein response. *Nature* **533**, 416 (2016).

44. Fessler, E. *et al.* A pathway coordinated by DELE1 relays mitochondrial stress to the cytosol. *Nature* **579**, 433–437 (2020).

45. Guo, X. *et al.* Mitochondrial stress is relayed to the cytosol by an OMA1–DELE1–HRI pathway. *Nature* **579**, 427–432 (2020).

46. Khan, N. A. *et al.* mTORC1 Regulates Mitochondrial Integrated Stress Response and Mitochondrial Myopathy Progression. *Cell Metab* **26**, 419-428 e5 (2017).

47. Picard, M. *et al.* Progressive increase in mtDNA 3243A>G heteroplasmy causes abrupt transcriptional reprogramming. *Proc Natl Acad Sci U S A* **111**, E4033-42 (2014).

48. McMillan, R. P. *et al.* Quantitative Variation in m.3243A > G Mutation Produce Discrete Changes in Energy Metabolism. *Sci. Rep.* **9**, 5752 (2019).

49. Chae, S. *et al.* A Systems Approach for Decoding Mitochondrial Retrograde Signaling Pathways. *Sci. Signal.* **6**, rs4 LP-rs4 (2013).

50. Civiletto, G. *et al.* Rapamycin rescues mitochondrial myopathy via coordinated activation of

autophagy and lysosomal biogenesis. *EMBO Mol Med* **10**, (2018).

51. Zheng, X. *et al.* Alleviation of neuronal energy deficiency by mTOR inhibition as a treatment for mitochondria-related neurodegeneration. *Elife* **5**, (2016).

52. Haroon, S. *et al.* Multiple Molecular Mechanisms Rescue mtDNA Disease in C. elegans. *Cell Rep* **22**, 3115–3125 (2018).

53. Johnson, S. C. *et al.* mTOR Inhibition Alleviates Mitochondrial Disease in a Mouse Model of Leigh Syndrome. *Science (80-.).* **342**, 1524 LP – 1528 (2013).

54. Barriocanal-Casado, E. *et al.* Rapamycin administration is not a valid therapeutic strategy for every case of mitochondrial disease. *EBioMedicine* **42**, 511–523 (2019).

55. White, H. E. *et al.* Accurate Detection and Quantitation of Heteroplasmic Mitochondrial Point Mutations by Pyrosequencing. *Genet. Test.* **9**, 190–199 (2005).

56. Schindelin, J. *et al.* Fiji: an open-source platform for biological-image analysis. *Nat. Methods* **9**, 676–682 (2012).

57. Rooney, J. P. *et al.* PCR based determination of mitochondrial DNA copy number in multiple species. *Methods Mol Biol* **1241**, 23–38 (2015).

58. Rehman, J. *et al.* Inhibition of mitochondrial fission prevents cell cycle progression in lung cancer. *FASEB J.* **26**, 2175–2186 (2012).

59. Yuneva, M., Zamboni, N., Oefner, P., Sachidanandam, R. & Lazebnik, Y. Deficiency in glutamine but not glucose induces MYC-dependent apoptosis in human cells . *J. Cell Biol.* **178**, 93–105 (2007).

60. Méndez-Lucas, A. *et al.* Identifying strategies to target the metabolic flexibility of tumours. *Nat. Metab.* **2**, 335–350 (2020).

61. Chong, J., Wishart, D. S. & Xia, J. Using MetaboAnalyst 4.0 for Comprehensive and Integrative Metabolomics Data Analysis. *Curr. Protoc. Bioinforma.* **68**, e86 (2019).

62. Listenberger, L. L. *et al.* Triglyceride accumulation protects against fatty acid-induced lipotoxicity. *Proc. Natl. Acad. Sci.* **100**, 3077 LP – 3082 (2003).

63. Varet, H., Brillet-Guéguen, L., Coppée, J.-Y. & Dillies, M.-A. SARTools: A DESeq2- and EdgeR-Based R Pipeline for Comprehensive Differential Analysis of RNA-Seq Data. *PLoS One* **11**,

e0157022 (2016).

64. Xia, J., Gill, E. E. & Hancock, R. E. W. NetworkAnalyst for statistical, visual and network-based meta-analysis of gene expression data. *Nat. Protoc.* **10**, 823–844 (2015).

ACKNOWLEDGEMENTS

We thank Ian Holt (Biodondostia Research Institute, San Sebastián, Spain) for sharing the A549 cybrid cell line with us, Michal Minczuk (MRC Mitochondrial Biology Unit, Cambridge, UK) for sharing the 143B cybrid cell lines, Benoit Bilanges (UCL Cancer Institute) for invaluable discussions and guidance, Alice Giustacchini (UCL ICH) for help with single-cell analyses, Stephanie Carrington (Division of Neuropathology, UCL IoN) for sectioning the muscle biopsies, and Metabolomics STP of the Francis Crick Institute for assistance with GC-MS analysis. We also acknowledge The MRC Centre for Neuromuscular Diseases Biobank (supported by the National Institute for Health Research Biomedical Research Centres at Great Ormond Street Hospital for Children NHS Foundation Trust and at University College London Hospitals NHS Foundation Trust and University College London) for providing all patient-derived cells used in this study. NP was supported by Marie Sklodowska-Curie Individual Fellowship (Horizon 2020 Grant No. 653434) RDSP is supported by a Medical Research Council Clinician Scientist Fellowship (MR/S002065/1). GS is supported by Telethon GGP16026 and CRUK Pioneer Award C28472/A29264. MY is supported by the Francis Crick Institute which receives its core funding from Cancer Research UK (FC001223), the UK Medical Research Council (FC001223), and the Wellcome Trust (FC001223). We also thank Action Medical Research for funding the early stages of this work and the Taiwan government for funding CYC's PhD Fellowship.